The influence of crystal electric field on the physical properties of $CeCd_3X_3$ (X = P and As)

by

Obinna Uzoh

M.Sc., Sungkyunkwan University, 2020
B.Sc., University of Nigeria, Nsukka, 2015

Thesis Submitted in Partial Fulfillment of the
Requirements for the Degree of
Master of Science

in the
Department of Physics
Faculty of Science

SIMON FRASER UNIVERSITY
Summer 2022

Declaration of Committee

Name:	**Obinna Uzoh**
Degree:	**Master of Science**
Thesis title:	**The influence of crystal electric field on the physical properties of $CeCd_3X_3$ (X = P and As)**
Committee:	**Chair:** Malcolm Kennett Associate Professor, Physics
	Eundeok Mun Supervisor Associate Professor, Physics
	Steve Dodge Committee Member Associate Professor, Physics
	Jeff Sonier Examiner Professor, Physics

Abstract

$CeCd_3As_3$ and $CeCd_3P_3$ compounds that adopt the hexagonal $ScAl_3C_3$-type structure are triangular lattice antiferromagnets. These compounds indicate antiferromagnetic ordering below ∼0.5 K. Although the magnetic contribution to the specific heat C_m increases significantly below 10 K, the electrical resistivity of $CeCd_3As_3$ and $CeCd_3P_3$ follows typical metallic behavior that is inconsistent with Kondo lattice systems. Also, these compounds display huge magnetic anisotropy due to the crystal electric field (CEF) effect. We have undertaken a CEF analysis to understand their ground state properties. Based on CEF analysis, the ground state is in mixed states of $|\pm 5/2\rangle$ and $|\mp 1/2\rangle$, with a dominant $|\mp 1/2\rangle$ character. The CEF analysis in the presence of a molecular field gives a reasonable agreement with experimental data and thus indicates that the moments of the Ce^{3+} ions in the *ab*-plane are in close exchange interaction.

Keywords: Crystal electric field; Point charge model; Ce-based compounds; Triangular lattice; Antiferromagnetism

Dedication

This thesis work is dedicated to my parents, my family, and my spouse.

Acknowledgements

I would like to thank my supervisor Dr. Eundeok Mun for taking the time and effort in guiding me throughout the entire period of this thesis work. Also, a special thank you to all my mentors, too numerous to mention, who have inspired my dream of becoming a scientist. Lastly, to my colleagues at the Emerging Materials Lab for fruitful discussions and assistance in making this thesis project a reality.

Table of Contents

List of Tables

List of Figures

Chapter 1

Introduction

1.1 Rare-earths

Materials in the lanthanide series (from lanthanum to lutetium), often including scandium and yttrium, show various magnetic and electronic properties that depend on the rare-earth element. Moreover, rare-earth-based compounds offer the realization of rich physics such as magnetism, superconductivity, Kondo effects, and large quantum spin fluctuations [1–6]. The electronic structure of the rare-earth elements is either of the form $[\mathrm{Xe}]4f^n5d^16s^2$ or $[\mathrm{Xe}]4f^{n+1}5d^06s^2$. The $5d$ and $6s$ are the outer shells and their electrons participate in chemical bonding, whereas the $4f$ shell is spatially localized and closer to the nucleus. Such localized nature of the $4f$ shell is responsible for many interesting properties observed in rare-earth-based materials [7]. The localized $4f$ orbital angular momentum L couples to the spin state S, and hence the electronic state is no longer independently described by the L and S state. Rather, the total angular momentum, $J = L + S$, becomes a good quantum number.

It is well known that in rare-earths, magnetism originates from the partially filled $4f$-shell electrons. Since these electrons are well localized, their magnetic moments are large. They are also characterized by strong single-ion magnetocrystalline anisotropy and relatively low magnetic ordering temperatures. The spin-orbit coupled ground states (Hund's rule ground states) are strongly influenced by the single-ion crystal electric field (CEF). By contrast, the magnetism exhibited by most transition metals is itinerant, which gives rise to lower magnetic moments and higher ordering temperatures. The $3d$ shell electrons experience much stronger CEF than the spin-orbit coupling, owing to the delocalized nature of the $3d$ state. Under the CEF, the L state in the $3d$ electron systems precesses and averages to zero, the orbital angular momentum is said to be quenched. Another way to put it is that L states are not eigenfunctions of the crystal field potential. Thus, S (to some approximation) is a good quantum number in the case of $3d$ systems [8].

1.2 Competing energy scales in Ce-based intermetallic compounds

Ce-based intermetallic systems have attracted considerable attention amongst the rare-earth-based compounds because of their interesting ground state properties, such as magnetic ordering [9], the Kondo effect [10], heavy fermion behavior [11], and large quantum spin fluctuations [12, 13]. Most of these phenomena originate from the $4f^1$ electron configuration of Ce^{3+} ion which gives rise to charge and spin fluctuation. When the localized $4f$-shell electrons are immersed in the sea of conduction electrons, Kondo screening can develop, and many Ce-based compounds show such a state. However, the f-electrons carry local moments, so the right way to describe the Ce-based Kondo lattice system is that magnetism and the Kondo effect can coexist, which can lead to unconventional superconductivity [14, 15], valence fluctuations [16], and quantum critical behavior [17–19]

One of the important energy scales in Ce-based intermetallic systems is associated with the hybridization strength between localized $4f$ electrons and conduction electrons. The hybridization strength is given by $\Gamma = \pi V_{fc}^2 N(\epsilon_F)$ [20], where V_{fc} is an appropriate average over the hybridization matrix element and $N(\epsilon_F)$ is the density of states at the Fermi level. Another important energy scale, E_{4f}, comes from the binding energy of the unperturbed $4f$ electrons [20].

Three cases can arise depending on which energy scale is dominant. The first case is when $\Gamma \gg E_{4f}$. Here, the $4f$ electrons are strongly hybridized with the conduction electrons. In this case, the $4f$ electrons are delocalized, lose their moments, and stay in an intermediate valence state. Ce-based systems in this regime are non-magnetic [20].

In the second case for which $\Gamma < E_{4f}$, there is a significant interaction between the $4f$ levels and the conduction bands which leads to the formation of Kondo singlets. In this regime, Ce-based intermetallic compounds show a logarithmic increase of resistivity (Kondo effect) and a highly enhanced electronic specific heat coefficient γ (heavy fermion states) [20].

Lastly, when $\Gamma \ll E_{4f}$, the hybridization strength is negligible. In this regime, the $4f$ electrons are well localized with a stable 3+ valence state in which many Ce-based systems display long-range magnetic ordering through the Ruderman-Kittel-Kasuya-Yoshida (RKKY) indirect exchange interaction [20].

1.3 Crystal electric field effect

The investigation of the crystal electric field (CEF) effect for $4f$ rare-earth-based intermetallic compounds is important to understand magnetism and magnetic materials both from theoretical point of view and for applications. For $4f$ systems, the spin-orbit coupling is stronger than the perturbation from the crystal field. However, the crystal field is still large

enough to lift the degeneracy of the ground state J multiplet, leading to very strong single-ion crystalline anisotropy− which is a preferential alignment of the magnetic moments in the crystal field [7,21]. When the degeneracy is partially or completely lifted, a great impact on magnetic susceptibility, specific heat, resistivity, and magnetization is expected. Therefore, magnetic susceptibility, specific heat, magnetization, and neutron diffraction can be used to obtain the CEF energy profile based on CEF theory.

The CEF theory involves the splitting of the energy states of an ion due to the electrostatic influence arising from neighboring ions in the crystal [21–23]. This influences the alignment of the magnetic moments in the crystal field, thus leading to a large anisotropy as the moments would prefer to align in one direction than others. The ground state of the $4f$ electrons is in a J multiplet with a $(2J+1)-$fold degeneracy. The CEF can split this degeneracy into various sub-states depending on the number of $4f$ electrons per ion according to the Kramers theorem. This theorem states that if the electron number is odd, then the total angular momentum J is half-integer. The minimum degeneracy in the ground state is 2; such a state is a doublet. These systems are so-called Kramers ions. On the other hand, if the electron number is even, then the total angular momentum J is an integer, and the degeneracy can be totally lifted. But in general, there is a mixture of singlet, doublet, triplet, and quartet states. These systems are so-called non-Kramers ions [21].

In addition, the CEF effect depends not only on the local symmetry of the $4f$ ions but also on the charge distribution of the surrounding ions. A very simplistic approach to describing such a charge distribution is the point charge model. In this model, the surrounding ions and the central ion are treated as point charges with electrostatic interaction between them [24]. Clearly, this model has some drawbacks. The first is that the spatial distribution of the charges of the ions is not put into consideration. Secondly, it neglects the exchange interaction and screening between electrons and ions. Lastly, it does not take into account the wavefunction overlap between the single-ion and the surrounding ions [24]. Nevertheless, it has been very successful in describing, qualitatively, the magnetic properties of various systems [25–29].

1.4 Magnetization and molecular field

A magnetic solid consists of a large number of atoms with magnetic moments. The magnetization $\vec{M}$ is defined as the magnetic moment per unit volume. For a linear material the magnetization is proportional to the applied field $\vec{H}$.

$$\vec{M} = \chi \vec{H}, \tag{1.1}$$

χ is called the magnetic susceptibility and it represents the magnetic moment induced by a magnetic field $\vec{H}$ per unit volume. When a magnetic field induces a magnetic moment which opposes the applied magnetic field that caused it, such phenomenon is known as dia-

magnetism. For a diamagnetic substance, there is a weak, negative magnetic susceptibility. All materials show some degree of diamagnetism. Paramagnetism corresponds to a positive susceptibility so that an applied magnetic field induces a magnetization which aligns parallel with the applied magnetic field which caused it [30, 31].

In some materials, there are interactions between magnetic moments that causes some preferential alignment of spins in the absent of field, thus forming an ordered ground state. In a ferromagnetic material, the magnetic moments are in parallel alignment. In an antiferromagnetic material, the adjacent magnetic moments lie in antiparallel alignment. Examples of other ground states are spiral and helical structures in which the direction of the magnetic moment precesses around a cone or a circle as one moves from one site to the next [30, 31]. The interactions between magnetic moments can be described, approximately, as arising from a molecular field $\vec{H}_{\mathrm{m}}$. The effect of the molecular field is to orient the spins even in the absent of applied field. In the mean-field approximation each magnetic moment experiences a molecular field proportional to the magnetization, and is given as

$$\vec{H}_{\mathrm{m}} = \lambda \vec{M}, \tag{1.2}$$

where λ is a constant (independent of temperature) that parametrizes the strength of the molecular field. For a simple paramagnet placed in a magnetic field, the total field becomes $\vec{H} + \vec{H}_{\mathrm{m}}$. Hence, at low temperature the moments can be aligned by the internal molecular field, even without any applied field being present.

The molecular field gives an approximate representation of the quantum mechanical Heisenberg exchange interaction $-\sum_{ij} \mathrm{J}_{ij} \vec{S}_i \cdot \vec{S}_j$, where J_{ij} represents the exchange integral and is related to the overlap of the charge distributions of the ions i, j with spins $\vec{S}_i, \vec{S}_j$ respectively.

1.5 Specific heat measurement and the Schottky anomaly

Measured specific heat C_p has both the electronic and lattice components. To understand the magnetic properties of materials it is important to extract the magnetic contribution of the specific heat C_m. This can be done by performing two specific heat measurements. The first measurements would be on the interested magnetic material, for example $CeCd_3As_3$. The second specific measurement would be on a non-magnetic isostructural analouge, for example $LaCd_3As_3$. C_m then is given as the difference between C_p for $CeCd_3As_3$ and C_p for $LaCd_3As_3$.

Although C_p generally increases with temperature, in some cases, the plot of C_m as a function of temperature T depict a broad peak (local maximum) at some temperatures. This effect is known as Schottky anomaly. The Schottky anomaly is associated with discrete energy levels coming from the splitting of energy states by effect such as crystal field, Zeeman, or molecular field. The Schottky anomaly arises due to the thermal transitions

of electrons to excited energy levels. At zero temperature only the lowest energy level is occupied, entropy is zero. As the temperature increases, the entropy increases as well. At a temperature corresponding to the energy difference between the energy levels there is a large build-up of entropy for a small change in temperature. This give rise to the broad peak in the specific heat C_m.

1.6 Outline of thesis

This thesis is concerned with the regime where the crystal field is dominant and thus plays a key role in describing the magnetic properties of various compounds. In general, the CEF applies to any magnetic system (for example, transition compounds with a d character and rare-earth compounds with an f character). In this thesis, the CEF effect in $4f$ systems would be explored.

This thesis is organized as follows. Chapter 2 establishes the theoretical framework for the CEF effect based on the point charge model. Chapter 3 presents the computational implementation of the CEF model alongside the steps in making a good CEF fit. In Chapter 4, the CEF analysis of $CeCd_3As_3$ and $CeCd_3P_3$ is presented and discussed. Lastly, a conclusion of the study is made in Chapter 5.

Chapter 2

Theoretical Background

In this chapter, a brief description of the point charge model is given, following Refs. [21,24]. Non-vanishing CEF parameters associated with the local point symmetries of magnetic ions surrounded by point charges are presented. Also, some physical quantities that can be calculated from the eigenvalues and eigenstates of the CEF Hamiltonian are introduced.

2.1 Point charge model

The CEF Hamiltonian can be built from the Coulomb interaction between the single magnetic ion and the neighboring ions in the crystal. In the simplest (point charge) model, constituent ions in the crystal are assumed to be point charges, ignoring the spatial charge distributions on the lattice.

Consider a $4f$ ion at position $\vec{r}$, close to the origin O, in a potential V_c produced by surrounding point charges at positions $\vec{R}_i$ as shown schematically in Fig. 2.1. From electromagnetic theory, such a potential V_c obeys the Laplace equation $\nabla^2 V_c = 0$, and hence can be written as

$$V_c(\vec{r}) = \frac{1}{4\pi\epsilon_0} \sum_i \frac{q_i}{|\vec{r} - \vec{R}_i|} \ , \tag{2.1}$$

where $1/\mid \vec{r} - \vec{R}_i \mid$ can be expanded in a series as

$$\frac{1}{|\vec{r} - \vec{R}_i|} = \frac{1}{\sqrt{(r^2 + R_i^2 - 2rR_i\cos\omega)}} = \frac{1}{R_i} \sum_{n=0}^{\infty} \left(\frac{r}{R_i}\right)^n P_n(\cos\omega) \ , \tag{2.2}$$

for all $r < R_i$, with ω denoting the angle between $\vec{r}$ and $\vec{R}_i$. The Legendre-polynomials $P_n(\cos\omega)$ can be expressed in terms of spherical harmonics Y_n^m as

$$P_n(\cos\omega) = \frac{4\pi}{2n+1} \sum_{m=-n}^{n} Y_n^m(\Omega_r)\, Y_n^{m*}(\Omega_R) \ . \tag{2.3}$$

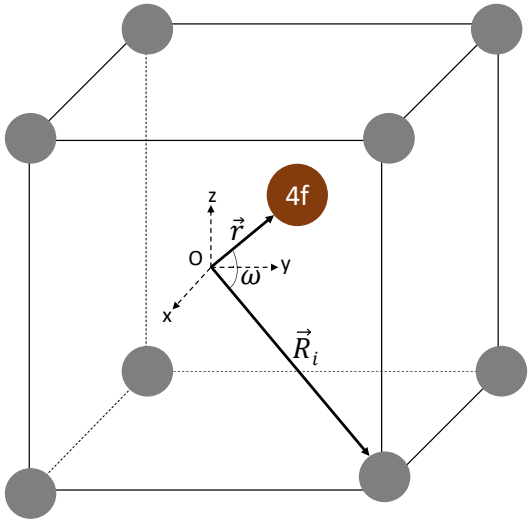

Figure 2.1: A $4f$ magnetic ion at a position $\vec{r}$ (brown circle) in a potential produced by eight neighboring point charges (grey circles), $\vec{R}_i$ is the position of the ith neighboring charge from the origin O. The angle between $\vec{r}$ and $\vec{R}_i$ is ω.

In order to avoid the complex numbers associated with the spherical harmonics, it is important to cast Eqn. 2.3 in terms of tesseral harmonics, Z_n^m, which are real, and defined according to Ref. [24] as

$$\begin{aligned} Z_n^0 &= Y_n^0, & m = 0 \\ Z_n^m &= \frac{1}{\sqrt{2}}\left[Y_n^{-m} + (-1)^m Y_n^m\right], & m > 0 \\ Z_n^m &= \frac{i}{\sqrt{2}}\left[Y_n^m - (-1)^m Y_n^{-m}\right], & m < 0 \ . \end{aligned} \tag{2.4}$$

Inserting the tesseral harmonics into Eqn. 2.3 leads to

$$V_c(\vec{r}) = \sum_{n=0}^{\infty}\sum_{m=-n}^{n} r^n Z_n^m(\Omega_r)\frac{1}{2n+1}\sum_i \frac{q_i Z_n^m(\Omega_R)}{\epsilon_0 R_i^{n+1}} \ . \tag{2.5}$$

By making use of the definitions

$$\gamma_n^m = \frac{1}{2n+1}\sum_i \frac{q_i Z_n^m(\Omega_R)}{\epsilon_0 R_i^{n+1}} \tag{2.6}$$

and

$$H_n^m = \sum_{j=1}^{N} r_j^n Z_n^m(\theta_j, \phi_j) \ , \tag{2.7}$$

the CEF Hamiltonian can be expressed as

$$\mathcal{H}_{CEF} = -|Q| \sum_{j}^{N} V_c(\vec{r}_j) = \sum_{n,m} \gamma_n^m H_n^m \ , \tag{2.8}$$

where the charge $Q = Ze$ of the ion, N is the total number of $4f$ ions, and $\vec{r}_j$ is the position of the jth $4f$ ion. It is convenient to represent the matrix element of $\mathcal{H}_{CEF}$ in terms of equivalent operators, as shown below. For example, consider the H_2^0 term which can be expanded (using the definition in Eqn. 2.7)

$$H_2^0 = \sum_j r_j^2 \sqrt{\frac{5}{4\pi}} \frac{1}{2} \left(2\cos^2\theta_j - 1 \right) = \sum_j r_j^2 \sqrt{\frac{5}{4\pi}} \frac{1}{2} \left(\frac{3z^2 - r_j^2}{r_j^2} \right) \ . \tag{2.9}$$

By making use of the following

$$\begin{aligned} x &= r\sin\theta\cos\phi \rightarrow J_x \\ y &= r\sin\theta\sin\phi \rightarrow J_y \\ z &= r\cos\phi \rightarrow J_z \\ r &\rightarrow |\vec{J}| \end{aligned}$$

and

$$\begin{aligned} xy &\rightarrow (1/2)(J_x J_y + J_y J_x) \\ J_\pm &= J_x \pm i J_y \ , \end{aligned}$$

the matrix element of H_2^0 within the ground state multiplet $|\Gamma\rangle$ of a $4f$ ion can be written as

$$\begin{aligned} \langle\Gamma|H_2^0|\Gamma\rangle &= \langle\Gamma| \sum_j r_j^2 \sqrt{\frac{5}{4\pi}} \frac{1}{2} \left(\frac{3z^2 - r_j^2}{r_j^2} \right) |\Gamma\rangle \\ &= \frac{5}{4\pi} \frac{1}{2} \alpha_J \langle r^2 \rangle \langle\Gamma| \left(3J_z^2 - J(J+1) \right) |\Gamma\rangle \ , \end{aligned} \tag{2.10}$$

with the radial matrix elements defined by

$$\langle r^n \rangle = \int |R_{4f}(r)|^2 r^{n+2} dr \tag{2.11}$$

and α_J, known as the Stevens factors, are listed in Table 2.1. The radial matrix elements of $4f$ radial wave functions R_{4f} have been calculated for different rare-earth atoms, as shown in Refs. [21, 32, 33].

Table 2.1: Rare-earth ions and their orbital (L), spin (S) and total angular momentum (J) quantum numbers, Landé factor g_J, and Stevens factors: $\Theta_n = \alpha_J$, β_J, γ_J (see Eqn. 2.18). Table taken from Ref. [21].

ion	L	S	J	g_J	$\alpha_J \times 10^2$	$\beta_J \times 10^4$	$\gamma_J \times 10^6$
Ce^{3+}	3	1/2	5/2	6/7	−5.7143	63.4921	0.0000
Pr^{3+}	5	1	4	4/5	−2.1010	−7.3462	60.9940
Nd^{3+}	6	3/2	9/2	8/11	−0.6428	−2.9111	−37.9880
Pm^{3+}	6	2	4	3/5	0.7713	4.0755	60.7807
Sm^{3+}	5	5/2	5/2	2/7	4.1270	25.0120	0.0000
Eu^{3+}	3	3	0	−	0.0000	0.0000	0.0000
Gd^{3+}	0	7/2	7/2	2	0.0000	0.0000	0.0000
Tb^{3+}	3	3	6	3/2	−1.0101	1.2244	−1.1212
Dy^{3+}	5	5/2	15/2	4/3	−0.6349	−0.5920	1.0350
Ho^{3+}	6	2	8	5/4	−0.2222	−0.3330	−1.2937
Er^{3+}	6	3/2	15/2	6/5	0.2540	0.4440	2.0699
Tm^{3+}	5	1	6	7/6	1.0101	1.6325	−5.6061
Yb^{3+}	3	1/2	7/2	8/7	3.1746	−17.3160	148.0001

Table 2.2: List of radial matrix elements $\langle r^n \rangle$ for $n = 2$, 4 and 6 for rare-earth ions [21].

ion	$\langle r^2 \rangle (\text{Å}^2)$	$\langle r^4 \rangle (\text{Å}^4)$	$\langle r^6 \rangle (\text{Å}^6)$
Ce^{3+}	0.3666	0.3108	0.5119
Pr^{3+}	0.3350	0.2614	0.4030
Nd^{3+}	0.3120	0.2282	0.3300
Pm^{3+}	0.2899	0.1991	0.2755
Sm^{3+}	0.2728	0.1772	0.2317
Eu^{3+}	0.2569	0.1584	0.1985
Gd^{3+}	0.2428	0.1427	0.1720
Tb^{3+}	0.2302	0.1295	0.1505
Dy^{3+}	0.2188	0.1180	0.1328
Ho^{3+}	0.2085	0.1081	0.1181
Er^{3+}	0.1991	0.0996	0.1058
Tm^{3+}	0.1905	0.0921	0.0953
Yb^{3+}	0.1826	0.0854	0.0863

By defining Stevens operators O_n^m according to Ref. [34], the operators which initially have spatial dependence are simply proportional to angular momentum operators. For example,

$$O_2^0 = \left(3J_z^2 - J(J+1)\right). \tag{2.12}$$

Note that the Stevens operators are different from the Stevens factors which are listed in Table 2.1. For each tesseral harmonic function the Stevens operator can be defined by substituting x, y and z by the components J_x, J_y and J_z, respectively. A complete list of these Stevens operators is given in the Appendix of Ref [21]. In addition, the coefficients of the polynomials in x, y and z in the definition of the tesseral functions (see the Appendix of Ref. [21]) are denoted by p_n^m; for example $p_2^0 = \frac{1}{2}\sqrt{\frac{5}{4\pi}}$.

Hence the matrix elements of the ground state multiplet of the $4f$ ion yields

$$H_2^0 = \sum_j r_j^2 \sqrt{\frac{5}{4\pi}} \frac{1}{2} \left(\frac{3z^2 - r_j^2}{r_j^2}\right) \tag{2.13}$$

$$\rightarrow p_2^0 \alpha_J \langle r^2 \rangle O_2^0(\vec{J}). \tag{2.14}$$

In general,

$$H_n^m = \sum_j r_j^n Z_n^m(\Omega_j) = p_n^m \Theta_n \langle r^n \rangle O_n^m(\vec{J}). \tag{2.15}$$

This leads to the well known equation for the CEF Hamiltonian

$$\mathcal{H}_{CEF} = \sum_{n,m} B_n^m O_n^m \tag{2.16}$$

where

$$B_n^m = -|Q| p_n^m \gamma_n^m \langle r^n \rangle \Theta_n \tag{2.17}$$

$$\Theta_n = \begin{cases} \alpha_J, & \text{if } n = 2 \\ \beta_J, & \text{if } n = 4 \\ \gamma_J, & \text{if } n = 6 \end{cases} \tag{2.18}$$

B_n^m are known as the CEF parameters, and can be determined from Eqn. 2.17 in the point charge model formalism. The variable γ_n^m is given in Eqn. 2.6. The additional parameters Θ_n and $\langle r^n \rangle$ are tabulated in Tables 2.1 and 2.2, respectively.

2.2 CEF parameters and point group symmetry

The CEF parameters in the Hamiltonian of Eqn. 2.16 depend on the point symmetry of the magnetic ion. In Eqn. 2.17, the full CEF parameters can be written as

$$B_n^m = -|Q|p_n^m \frac{1}{2n+1} \sum_i \frac{q_i Z_n^m(\Omega_R)}{\epsilon_0 R_i^{n+1}} \langle r^n \rangle \Theta_n \ , \tag{2.19}$$

where $Q = Ze$ is the charge of the central ion (as stated in the previous section); p_n^m are the coefficients of the tesseral harmonics (see the Appendix in Ref. [21]); R_i is the position of the ith surrounding charge from the point of symmetry O; $\langle r^n \rangle$ is the radial matrix element of the central ion; q_i is the charge of the ith surrounding charge; and Θ_n are the Stevens factors defined in Eqn. 2.18 and listed in Table 2.1.

Using the relationship between the tesseral harmonics and the spherical harmonics (Eqn. 2.4), B_n^m can be rewritten as

$$B_n^m = \begin{cases} -|Q|p_n^0 \dfrac{1}{2n+1} \displaystyle\sum_i \dfrac{q_i Y_n^0}{\epsilon_0 R_i^{n+1}} \langle r^n \rangle \Theta_n, & \text{if } m = 0 \\ -|Q|p_n^m \dfrac{1}{2n+1} \displaystyle\sum_i \dfrac{q_i \frac{1}{\sqrt{2}} \left[Y_n^{-m} + (-1)^m Y_n^m \right]}{\epsilon_0 R_i^{n+1}} \langle r^n \rangle \Theta_n, & \text{if } m > 0 \\ -|Q|p_n^m \dfrac{1}{2n+1} \displaystyle\sum_i \dfrac{q_i \frac{i}{\sqrt{2}} \left[Y_n^{m} - (-1)^m Y_n^{-m} \right]}{\epsilon_0 R_i^{n+1}} \langle r^n \rangle \Theta_n, & \text{if } m < 0 \ . \end{cases} \tag{2.20}$$

In Eqn. 2.20 all other terms can be non-zero except for the spherical harmonic term, which can be zero or non-zero depending on the point symmetry. Hence, the presence of the CEF parameter, B_n^m, is dependent on whether the spherical harmonics, Y_n^m, vanishes for a particular n, m

For example, consider an ion with cubic point symmetry surrounded by eight neighboring ions as shown in Fig 2.2. The ions are at the same distance d from the point of symmetry, but their angular coordinates are different for each ion. There are ions at $(d, \theta, \pi/4)$; $(d, \theta, 3\pi/4)$; $(d, \theta, 5\pi/4)$; $(d, \theta, 7\pi/4)$; $(d, (\pi - \theta), \pi/4)$; $(d, (\pi - \theta), 3\pi/4)$; $(d, (\pi - \theta), 5\pi/4)$; $(d, (\pi - \theta), 7\pi/4)$, where $\theta = \tan^{-1}\sqrt{2}$.

Begin by considering the term B_2^2. Since B_2^2 depends on $\frac{1}{\sqrt{2}}\left[Y_2^{-2} + Y_2^2\right]$, as seen in Eqn. 2.20, this term needs to be expanded for each ion and then summed over all eight contributions.

Employing the relation for the spherical harmonics [35], $Y_2^2 \approx \sin^2\theta e^{2i\phi}$ and $Y_2^{-2} \approx \sin^2\theta e^{-2i\phi}$, the term can be simplified as

$$\begin{aligned} \frac{1}{\sqrt{2}}\left[Y_2^{-2} + Y_2^2\right] &\approx \sin^2\theta \left(e^{-2i\phi} + e^{2i\phi}\right) \\ &= 2\sin^2\theta\cos(2\phi) \ . \end{aligned} \tag{2.21}$$

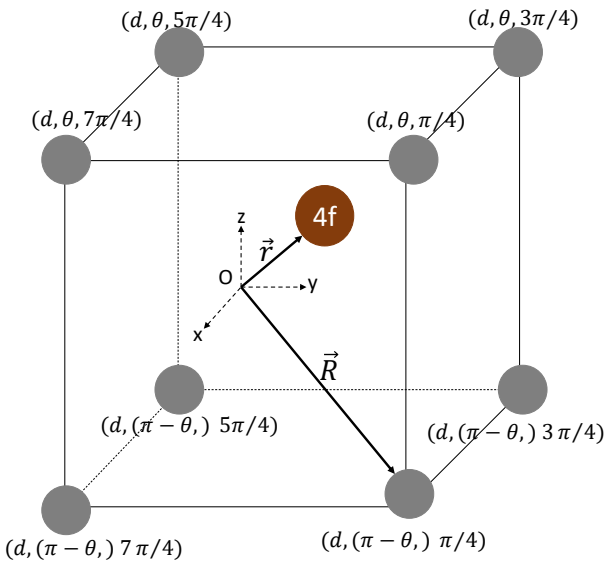

Figure 2.2: A magnetic ion (brown circle) in a cubic point symmetry surrounded by eight neighboring point charges (grey circles) at a fixed distance d from the origin O at varying angular coordinates.

For the given cubic point symmetry $\phi = \frac{k\pi}{4}$ with $k = 1, 3, 5, 7$, $\cos(2\phi) = 0$. Therefore, $\frac{1}{\sqrt{2}}\left[Y_2^{-2} + Y_2^2\right] = 0$ for each ion, so the B_2^2 term completely vanishes. Using the same procedure, it is easy to see that B_2^{-2} vanishes as well.

Having seen that in a cubic symmetry the $B_2^{\pm 2}$ term vanishes, consider the B_4^4 term. Here,

$$\begin{aligned}\frac{1}{\sqrt{2}}\left[Y_4^{-4} + Y_4^4\right] &\approx \sin^4\theta\left(e^{-4i\phi} + e^{4i\phi}\right) \\ &= 2\sin^4\theta\cos(4\phi)\ .\end{aligned} \tag{2.22}$$

For a cubic symmetry with $\phi = \frac{k\pi}{4}$ (where $k = 1, 3, 5, 7$), $\cos(4\pi) = -1$. The term $\frac{1}{\sqrt{2}}\left[Y_4^{-4} + Y_4^4\right]$ is non-zero, and therefore the B_4^4 does not vanish. However, the B_4^{-4} parameter vanishes:

$$\begin{aligned}\frac{i}{\sqrt{2}}\left[Y_4^{-4} - Y_4^4\right] &\approx i\sin^4\theta\left(e^{-4i\phi} - e^{4i\phi}\right) \\ &= -2i\sin^4\theta i\sin(4\phi)\ ,\end{aligned} \tag{2.23}$$

where $\sin(4\phi) = 0$ with $\phi = \frac{k\pi}{4}$ $(k = 1, 3, 5, 7)$, yielding $\frac{i}{\sqrt{2}}\left[Y_4^{-4} - Y_4^4\right] = 0$.

By applying this procedure to all CEF parameters for eightfold coordination, the vanishing CEF parameters are B_2^0, $B_2^{\pm 1}$, $B_2^{\pm 2}$, $B_4^{\pm 1}$, $B_4^{\pm 2}$, $B_4^{\pm 3}$, B_4^{-4}, $B_6^{\pm 1}$, $B_6^{\pm 2}$, $B_6^{\pm 3}$, B_6^{-4},$B_6^{\pm 5}$, and $B_6^{\pm 6}$. Therefore, in this cubic point symmetry only the CEF parameters B_4^0, B_4^4, B_6^0, and B_6^4 (see Table 2.3 cubic T_d, O, O_h) need to be considered.

Such local symmetry considerations of the point charge (as seen for a cubic symmetry case) require that some CEF parameters vanish while others are non-zero. This then allows the compilation of Table 2.3, where the non-vanishing CEF parameters for all crystallographic point groups are given [21].

2.3 Determination of the CEF parameters

The CEF parameters can be determined from first principles using the point charge model through Eqn. 2.17. In Eqn. 2.17 the CEF parameters do not depend on the crystal structure but highly rely on the local point symmetry of the magnetic ion. However, there is often a discrepancy between the theoretical calculation and the experimental result due to deviations from perfect crystalline material. For example, the lattice parameters and atomic positions in the model are not exactly the same as those in a real sample, and the point charge model itself ignores the spatial charge distributions of constituent ions. Hence, in general, the CEF parameters determined from a theoretical first-principles calculation do not reliably capture experimental data.

A more reliable method to determine CEF parameters is by fitting the experimental data, such as those obtained from neutron scattering and magnetic susceptibility, where the initial set of CEF parameters can be either obtained from the calculations of Eqn. 2.17 or deduced from the magnetic susceptibility measurement. The latter procedure is used in this thesis. It has been shown that the anisotropic magnetic susceptibility is mainly related to the first term of the CEF parameter B_2^0. In other words, the B_2^0 parameter gives a measure of the strength of the magnetocrystalline anisotropy and can be expressed in terms of the paramagnetic Weiss temperatures. For example, the B_2^0 term in tetragonal systems [36, 37] is given by

$$B_2^0 = (\theta_a - \theta_c)\frac{10k_B}{3(2J-1)(2J+3)} \ , \tag{2.24}$$

where k_B is the Boltzmann constant and J is the total angular momentum quantum number for a free rare-earth ion. The variables θ_a and θ_c are the paramagnetic Weiss temperatures for field applied along the a-axis and c-axis, respectively. θ_a and θ_c are obtained from the high temperature magnetic susceptibility data. By using Eqn. 2.24, one can find B_2^0, and then set it as a starting point for performing CEF fit. When eigenvalues and eigenstates of the CEF Hamiltonian are determined by fitting the magnetic susceptibility curves, physical observables such as magnetization, entropy, specific heat, and neutron spectra can be calculated. In the following, equations describing these physical properties are presented. In addition, a detailed procedure for this fitting scheme is discussed in Chapter 3, Computational methodology.

Table 2.3: Point group symmetries and their associated non-zero CEF parameters [21].

symmetry		B_2^0	$B_2^{\pm1}$	$B_2^{\pm2}$	B_4^0	$B_4^{\pm1}$	$B_4^{\pm2}$	$B_4^{\pm3}$	$B_4^{\pm4}$	B_6^0	$B_6^{\pm1}$	$B_6^{\pm2}$	$B_6^{\pm3}$	$B_6^{\pm4}$	$B_6^{\pm5}$	$B_6^{\pm6}$
triclinic	C_i C_1	+	±	±	+	±	±	±	±	+	±	±	±	±	±	±
monoclinic	C_2 C_s C_{2h}	+		±	+		±		±	+		±		±		±
rhombic	C_{2v} D_2 D_{2h}	+		+	+		+		+	+		+		+		+
tetragonal	C_4 S_4 C_{4h}	+			+				±	+				±		
tetragonal	D_4 C_{4v} D_{2d} D_{4h}	+			+				+	+				+		
trigonal	C_3 S_6	+			+			±		+			±			±
trigonal	D_3 C_{3v} D_{3d}	+			+			+		+			+			+
hexagonal	C_6 C_{3h} C_{6h}	+			+					+						±
hexagonal	D_6 C_{6v} D_{3h} D_{6h}	+			+					+						+
cubic	T T_h				+				+	+		+		+		+
cubic	T_d O O_h				+				+	+				+		
icosahedral	I_h									+					+	

2.4 Calculating physical properties from CEF

When the CEF parameters B_n^m are determined from the fit of magnetic susceptibility data, other physical quantities associated with CEF effects can be calculated. In this section, the relationships for deriving magnetization and entropy are presented.

2.4.1 Magnetization and magnetic susceptibility

The CEF Hamiltonian given in Eqn. 2.16 is not sufficient to calculate the magnetization. Two additional terms are necessary. The first term is to account for the external field's coupling to the ions' magnetic moments. Such a term is expressed as the Zeeman effect. The second term originate from the interaction between magnetic moments through a molecular field λM, λ is the molecular field parameter and M corresponds to the magnetization.

Mathematically, the total Hamiltonian takes the form

$$\mathcal{H} = \mathcal{H}_{CEF} - g_J \mu_B J_i (H_i + \lambda_i M_i) \quad (i = x, y, z - \text{directions}). \tag{2.25}$$

The first term $\mathcal{H}_{CEF}$ is the CEF Hamiltonian given by Eqn. 2.16, the second term is the Zeeman interaction, and the third term is the molecular field term. J_i is the angular momentum operator in the $i = x, y, z-$components, g_J is the Lande g-factor, and μ_B is the Bohr Magneton. The eigenvalues, E_n, and eigenstates, $|\Gamma_n\rangle$, are determined by diagonalizing the total Hamiltonian $\mathcal{H}$.

The magnetization is given by the expectation value of the magnetic moments

$$M_i = g_J \mu_B \sum_n \langle \Gamma_n | J_i | \Gamma_n \rangle \frac{e^{\frac{-E_n}{k_B T}}}{Z}, \tag{2.26}$$

where $Z = \sum_n e^{\frac{-E_n}{k_B T}}$ is the partition function. In the absence of a molecular field, the magnetization is given by Eqn. 2.26, where E_n and $|\Gamma_n\rangle$ are determined by diagonalizing the Hamiltonian only with the CEF and Zeeman term.

However, when the molecular field term $\lambda_i M_i$ is considered, the magnetization M_i (given in Eqn. 2.26) can be determined as follows. Note that on the right hand side (RHS) of Eqn. 2.26, E_n and $|\Gamma_n\rangle$ are gotten by diagonalizing the total Hamiltonian given in Eqn. 2.25 which depends on M_i. In other words, the RHS of Eqn. 2.26 is a function of M_i ($f(M_i)$). Hence, in the presence of molecular field, Eqn. 2.26 can be re-written as:

$$M_i = f(M_i) \tag{2.27}$$

Equation 2.27 is a nonlinear equation in which M_i can be calculated through a root-finding method.

In the absence of the molecular field term, the magnetic susceptibility can be calculated by

$$\chi^i_{CEF} = \frac{\partial M_i}{\partial H_i} \ , \tag{2.28}$$

where M_i is the magnetization (calculated when $\lambda_i = 0$) along the applied field direction and H_i is the applied field in three directions ($i = x, y, z$).

The magnetic susceptibility including the molecular field contribution is given by

$$\chi_i^{-1} = \left(\chi^i_{CEF}\right)^{-1} - \lambda_i \ . \tag{2.29}$$

2.4.2 Specific heat and entropy

The specific heat can be calculated from the free energy of the system, $F = -k_B T \ln Z$, by using the relation

$$C_m = -T\frac{\partial^2 F}{\partial T^2} \ . \tag{2.30}$$

The calculated specific heat only reflects the Schottky contributions which originate from the thermal population of the various CEF energy levels.

The magnetic entropy measures the degrees of freedom of a particular system. From thermodynamic relations, the magnetic entropy, defined as $S_m = k_B \ln Z$, can be obtained by

$$S_m = -\frac{\partial F}{\partial T} \ . \tag{2.31}$$

Chapter 3

Computational Methodology

The previous chapter introduces the theoretical framework for CEF effect based on the point charge model. Physical property calculations under the influence of CEF effects can be implemented by various computational programs [38–43]. These programs are often limited to fit only certain types of data and to calculate only specific physical quantities.

Recently, the *PyCrystalField* program based on the point charge model [44] has been developed, which provides capabilities for calculating and fitting various kinds of experimental data, like inelastic neutron spectrum, susceptibility, magnetization, and specific heat. Because the *PyCrystalField* is written in Python, it is easy to modify.

To adapt the *PyCrystalField* program to this thesis work, some modifications have been carried out. In this chapter, these modifications are discussed. In addition, a general procedure of carrying out a fit to experimental data and calculating relevant thermodynamic properties are presented. Lastly, multiple examples are shown to verify whether the modified CEF program works well.

3.1 Modification of program

3.1.1 Susceptibility fitting

The CEF excitations in a system can be captured by multiple experimental data. One way to obtain the CEF parameters is to fit the inelastic neutron spectrum, which is default method of fitting in the *PyCrystalField* package. On the other hand, the magnetic anisotropy arising from CEF effects is usually captured in susceptibility measurements. Thus, a fitting of the susceptibility data is another approach to determining the CEF parameters. In this thesis work, rather than fitting neutron spectrum data, we fit inverse susceptibility curves instead. This modification can be easily made since the *PyCrystalField* program offers the freedom to fit various kinds of experimental data.

The least-square cost function for fitting experimental data is modified from the neutron spectrum to inverse magnetic susceptibility. Note that the least-square cost function conven-

tionally denoted as χ^2 is denoted here as Δ^2 to avoid confusion with magnetic susceptibility χ. The least-square cost function Δ^2 is given as

$$\Delta^2 = \left(\chi^{-1}_{\text{data}} - \chi^{-1}_{\text{cal}}\right)^2, \tag{3.1}$$

where χ^{-1}_{data} is the experimental inverse susceptibility and χ^{-1}_{cal} is the calculated inverse susceptibility that can be determined using Eqn. 2.28 or Eqn. 2.29.

3.1.2 Global minimization

The least-square cost function, Δ^2, should be minimized to yield relevant CEF parameters. The aim of minimizing Δ^2 is to find unique sets of CEF parameters that reproduce the experimental data. There are several procedures to minimize Δ^2 while carrying out the CEF fit. With the help of the Scipy Python library, the *PyCrystalField* program incorporates both local and global minimization procedures. The local approach is very sensitive to the initial set of CEF parameters and does not yield a unique set of CEF parameters. However, the global optimization algorithm searches for a global minimum by performing random perturbations over basins followed by a minimization on each basin, yielding a unique set of CEF parameters. Thus, in this thesis work, the global minimization technique based upon the basin-hopping algorithm [45] is used to fit magnetic susceptibility curves to obtain the CEF parameters.

3.1.3 Molecular field

In many magnetic systems, it is important to account for the exchange interaction between magnetic ions. The magnetic moments interact with one another through a molecular field which is proportional to the average magnetization. Now, it is known that the origin of the molecular field is a quantum mechanical exchange interaction. The *PyCrystalField* program does not include the exchange interaction in the Hamiltonian. Therefore, the molecular field term based on the mean-field approximation [30, 31] is incorporated.

The full Hamiltonian $\mathcal{H}$, including the Zeeman term and molecular field term, is used in the program as follows

$$\mathcal{H} = \sum_{n,m} B^m_n O^m_n - g_J \mu_B J_i H_i - g_J \mu_B J_i \lambda_i M_i \quad (i = x, y, z - \text{directions}). \tag{3.2}$$

The last term represents the molecular field contribution. $\lambda_i M_i$ is called the molecular field, where the effective molecular interaction is parameterized as λ_i. The eigenvalues and eigenstates can be determined by diagonalizing the full Hamiltonian $\mathcal{H}$. The net magnetization M_i can be determined by solving Eqn. 2.27 using a root-finding technique such as the secant method or the Newton method.

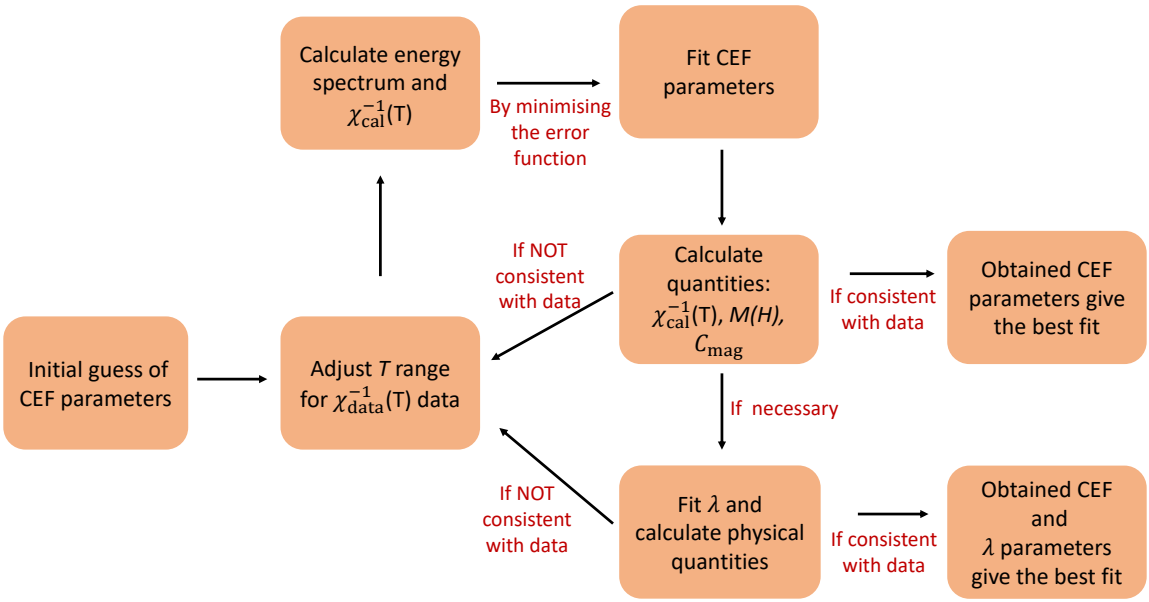

Figure 3.1: A schematic diagram of the CEF fitting procedure

3.2 Fitting procedure

A step-by-step process of performing a CEF fitting with the modified program is presented below.

1. Obtain the initial guess of the CEF parameters. Estimate leading CEF parameter (for example B_2^0 term given in Eqn. 2.24) from the inverse magnetic susceptibility curves. Other CEF parameters can be initialized to zero.

2. Properly choose the temperature range for fitting based on the inverse magnetic susceptibility data χ^{-1}_{data} (see section 3.4 on details for selecting temperature ranges).

3. Diagonalize the Hamiltonian to obtain the energy eigenstates and eigenvalues and calculate the inverse susceptibility, χ^{-1}_{cal}.

4. Determine the CEF parameters by minimizing the error function given in Eqn. 3.1.

5. Calculate magnetic susceptibility, magnetization, and specific heat by using the determined CEF parameters.

6. If the molecular field is not necessary, skip this step. Otherwise, include the molecular field term (Eqn. 2.29) and recalculate the physical quantities with λ_i.

7. Compare plots of the above calculated physical quantities to experimental data. If there is a good agreement, the best CEF and molecular field parameters are deter-

mined. If not, the process is repeated from step 2 until there is a consistency between the calculated and measured data.

A schematic diagram of this fitting procedure is shown in Fig. 3.1.

3.3 Program tests

As with any new program, it is important to ensure that the program is reliable to work with. The CEF program must be robust enough to handle various kinds of input data and be able to compute the correct output. In this section, we present the validity of the modified CEF program tested by comparing with some literature results. First, the code for numerical calculations is checked with already known CEF schemes. Next, the code for global minimization is tested.

3.3.1 CEF calculation of $CeAgSb_2$ magnetic properties

To check the CEF numerical calculations, we choose the CEF scheme of $CeAgSb_2$. The CEF analysis of the magnetic properties of $CeAgSb_2$ has been previously carried out [28]. Such analysis shows that the anisotropy in the high field magnetization is well explained by the presence of CEF. In particular, magnetization isotherms of $CeAgSb_2$ show complex metamagnetic transitions that arise from CEF energy level crossings [28].

$CeAgSb_2$ crystallizes in the tetragonal $ZrCuSi_2-$type structure ($P4/nmm$) and the Ce ions in this structure have a tetragonal point symmetry. In this configuration, the CEF Hamiltonian needs only B_2^0, B_4^0, and B_4^4 CEF parameters. Note that there are no B_6^0 and B_6^4 terms in the Hamiltonian, which are typically required for the tetragonal point symmetry. This is because the sixth-order Stevens factor, γ_J, vanishes for Ce^{3+} ($J = 5/2$), see Table 2.1.

We reproduce the magnetic susceptibility, specific heat, and magnetization (at 1.5 K and 20 K) calculations, as shown in Figs. 3.2 (a)−(d). The reported values of the parameters from Ref. [28] are used: $B_2^0 = 7.55$ K, $B_4^0 = -0.02$ K, $B_4^4 = -0.64$ K, $\lambda_x = -28$ mole/emu for $H \parallel ab$, and $\lambda_z = 0$ for $H \parallel c$. After diagonalizing the Hamiltonian, the eigenstates and eigenvalues are identical with those in Ref. [28]. The shape and magnitude of the anisotropic inverse susceptibility curves are well reproduced, as shown in Fig. 3.2 (a). The magnetic part of the specific heat indicates a broad maximum around 30 K, consistent with the previous report, as displayed in Fig. 3.2 (b). In addition, the metamagnetic transitions are captured very well (see Fig. 3.2 (c)). Thus, the program works well for numerical calculations of the physical quantities of $CeAgSb_2$.

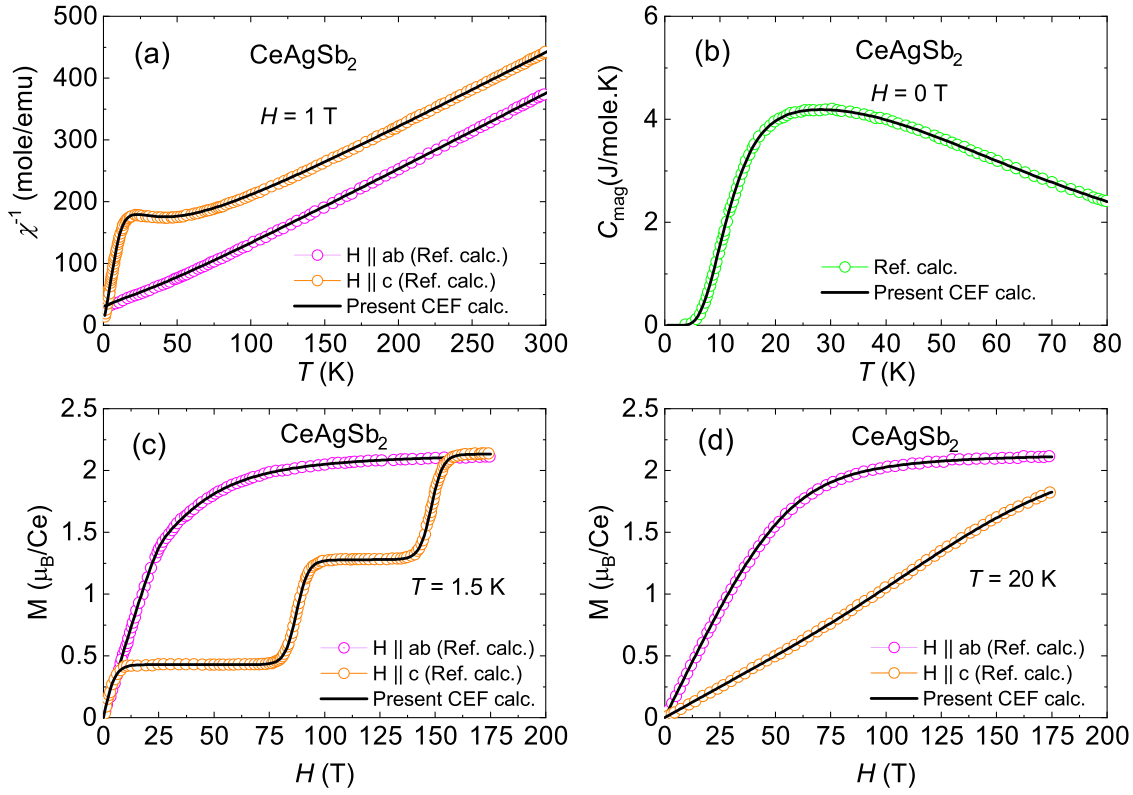

Figure 3.2: CEF calculation of the physical properties of $CeAgSb_2$ based on our CEF program as compared with the CEF scheme of Ref. [28]. Open symbols are from the reference calculations (digitized) and thin-black lines are calculations from our CEF program. (a) Inverse susceptibility plot. (b) Magnetic specific heat. (c) Magnetization at $T = 1.5$ K. (d) Magnetization at $T = 20$ K.

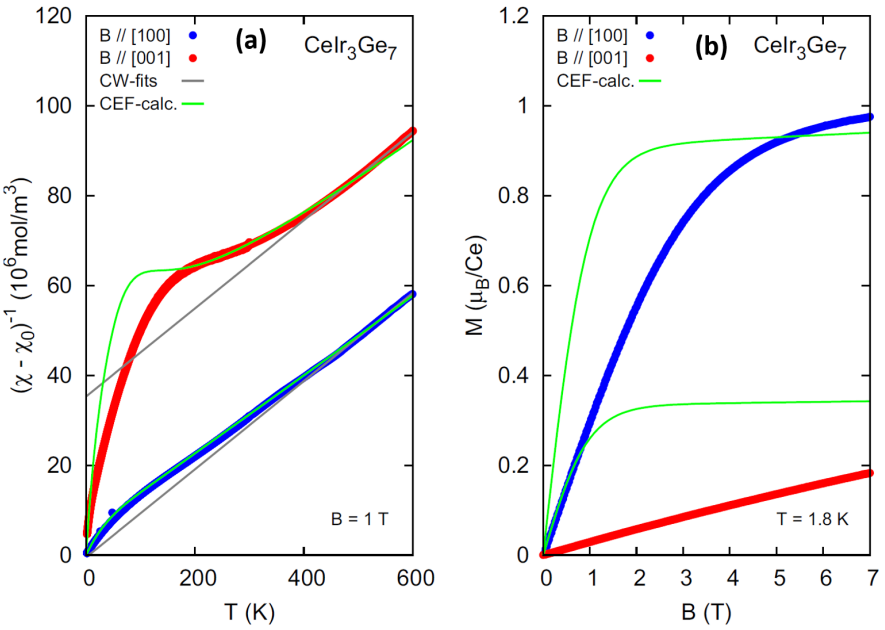

Figure 3.3: CEF fitting results for $CeIr_3Ge_7$ from Ref. [46]. Green lines are CEF calculations from the reference. (a) Inverse magnetic susceptibility at 1 T, grey lines are Curie-Weiss fits. (b) Isothermal magnetization at $T = 1.8$ K.

3.3.2 CEF fitting of $CeIr_3Ge_7$

Next, we check the code for global minimization with the results of $CeIr_3Ge_7$, taken from Ref. [46]. Figure 3.3 shows the inverse magnetic susceptibility and magnetization of $CeIr_3Ge_7$ plots from Ref. [46], where green lines represent their CEF calculations. Notice that unlike the magnetic susceptibility result (Fig. 3.3(a)), the CEF calculation for magnetization poorly agree with the the experimental data, as shown in Fig. 3.3(b).

Their CEF parameters (see Table 3.1), obtained by fitting the inverse magnetic susceptibility curves, are $B_2^0 = 34.40$ K, $B_4^0 = 0.82$ K, and $B_4^3 = 67.30$ K, resulting in a very large CEF energy level splittings of the first (374 K) and second excited level (1398 K).

Table 3.1: $CeIr_3Ge_7$: Comparing the CEF parameters, eigenvalues, and eigenstates.

	Ref. [46]	Present CEF scheme
CEF parameters (K):		
B_2^0	34.40	35.80
B_4^0	0.82	0.99
B_4^3	67.30	69.00
Energy level splitting:		
	374 K and 1398 K	343 K and 1434 K
Ground state:		
$\|\Gamma\rangle$	$0.54\|\pm 5/2\rangle - 0.84\|\mp 1/2\rangle$	$0.54\|\pm 5/2\rangle \mp 0.84\|\mp 1/2\rangle$

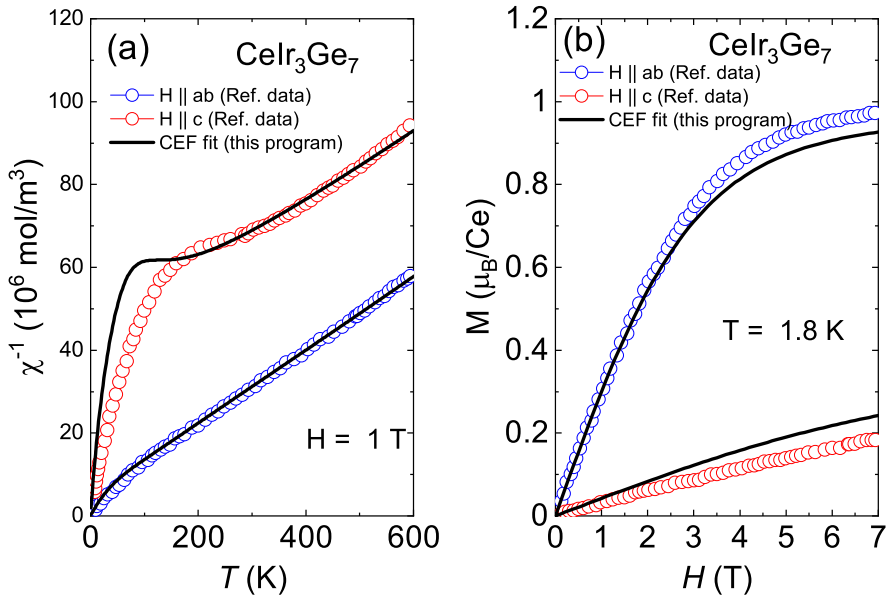

Figure 3.4: Present program CEF fit for $CeIr_3Ge_7$. Black lines are CEF calculations from fitting the reference inverse magnetic susceptibility data. Open symbols are data (digitized) from Ref. [46]. (a) Inverse magnetic susceptibility at 1 T. (b) Isothermal magnetization at $T = 1.8$ K.

In particular, due to the B_4^3 term the ground state wavefunctions are mixed between the $|\pm 5/2\rangle$ and $|\mp 1/2\rangle$ given as $|\Gamma\rangle = 0.54|\pm 5/2\rangle - 0.84|\mp 1/2\rangle$ [46].

To reproduce these results using our CEF fitting scheme, we first digitized the experimental data in Ref. [46] and then fit the inverse susceptibility data following the steps outlined in Sec. 3.2. Figure 3.4(a) shows the fit of the inverse magnetic susceptibility. The characteristics of the inverse magnetic susceptibility curves can be described by the CEF effect, especially the hump around 200 K, which are consistent with the results shown in Fig. 3.3(a). For the isothermal magnetization, CEF calculations in this study reproduced the essential features of the magnetization curves, as shown in Fig. 3.4(b). The almost linear field dependence of $M(H)$ for $H \parallel c$ is captured by our CEF fit. For $H \parallel ab$, the Brillouin function-like magnetization curve is reproduced. In this study, the CEF parameters are obtained to be $B_2^0 = 35.80$ K, $B_4^0 = 0.99$ K, and $B_4^3 = 69.00$ K, which are consistent with those obtained in Ref. [46]. The energy level splittings have values of 343 K and 1434 K, and the ground state is given as $|\Gamma\rangle = 0.54|\pm 5/2\rangle \mp 0.84|\mp 1/2\rangle$, which are also consistent with the reference (see Table 3.1). The small difference in magnitude between their reported CEF profile (CEF parameters and energy levels) and the CEF profile in this present study maybe due to the use of digitized data in carrying out our fitting. Therefore, the consistency of our CEF profile with the reference results indicate that our fitting scheme works well.

It is important to note that, although the CEF profile and inverse magnetic susceptibility plot are well reproduced, there is disagreement between the magnetization plots

(see Fig. 3.3(b) and Fig. 3.4(b)). To check this discrepancy, we used the CEF parameters of Ref. [46] to re-calculate their magnetization. The magnetization curves calculated does not match the reference calculations shown in Fig. 3.3(b). Hence, this discrepancy most probably comes from the nature of the numerical calculations employed in Ref. [46].

We also tested our modified CEF program with other rare-earth based compounds (other than Ce-based compounds), such as $ErAl_2Ge_2$ [47], $PrRhIn_5$ [29], $TbRhIn_5$ [29] compounds. For $ErAl_2Ge_2$ [47], the CEF Hamiltonian was based on a hexagonal site symmetry for the Er ions, where the CEF parameters are B_2^0, B_4^0, B_6^0, and B_6^6. Using the reported CEF parameters with molecular field parameters, our program reproduced their susceptibility, magnetization, and specific heat plots. Also, our program also works well in reproducing the CEF results of $PrRhIn_5$ [29] and $TbRhIn_5$ [29] in the presence of molecular field, where Pr and Tb ions have tetragonal symmetry with five CEF parameters: B_2^0, B_4^0, B_4^4, B_6^0, and B_6^4.

Therefore, based on the tests using these several rare-earth ions and symmetries, we have evaluated our modified program to perform well in calculating and fitting CEF parameters.

3.4 General comments on making a good CEF fit

In this chapter, we have described the CEF program that implements the CEF calculation and fitting. In addition, we presented some examples to evaluate the accuracy of our fitting scheme. Here, we shall comment on important factors that are necessary to make successful CEF fit.

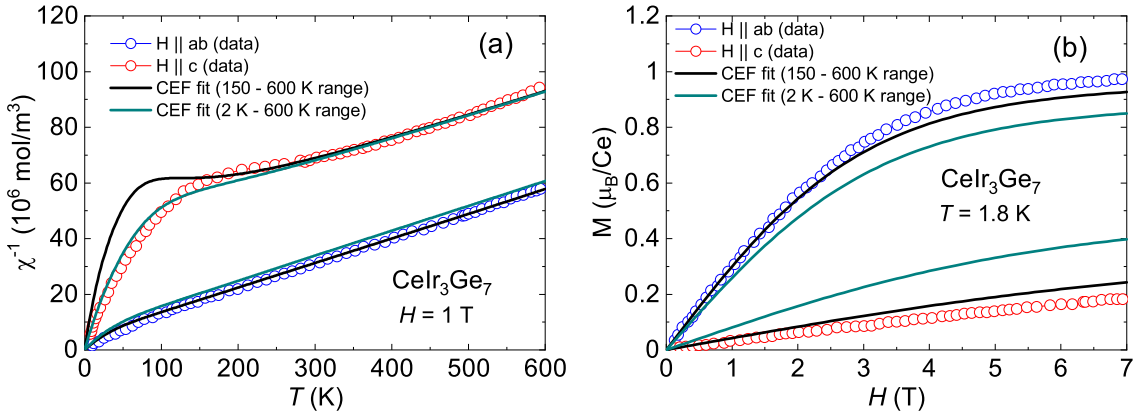

Figure 3.5: $CeIr_3Ge_7$ CEF fitting performed based on two different fitting ranges. The data was gotten from Ref. [46]. (a) Inverse magnetic susceptibility at 1 T. (b) Isothermal magnetization at 1.8 K.

First, in some magnetic systems the inclusion of exchange interaction to the CEF Hamiltonian is crucial in reproducing the magnetic properties. Hence, a good CEF fit can be only achieved if exchange interaction is taken into account.

Another important factor in producing a good CEF fit is the tuning of the temperature range of the inverse susceptibility data. As stated in Sec. 3.1.1, our CEF program fits the experimental data of inverse magnetic susceptibility to obtain a set of CEF parameters. Since the inverse magnetic susceptibility depends on temperature, the set of fitted CEF parameters would depend on fitting ranges of temperatures.

Figure 3.5 shows the CEF fits based on two different fitting ranges: one with the fitting range 150 K − 600 K and the other one with the range 2 K − 600 K. As shown in Fig. 3.5(a), for $H \parallel ab$, the calculated magnetic susceptibility curves for both temperature ranges well follow the experimental data. For $H \parallel c$ it is obvious that $\chi^{-1}(T)$ for fitting 2 K − 600 K gives a better description of experimental data than that for fitting 150 K − 600 K. However, when magnetization curves are compared, the fitting range of 150 K − 600 K gives a better agreement with the experimental data, as shown in Fig. 3.5(b). Hence, one can choose the 150 K − 600 K fitting range as it better describes both $\chi^{-1}(T)$ and $M(H)$ experimental data. Therefore, it is crucial to ensure that the temperature range used in the fitting gives the best set of CEF parameters.

However, in some cases, it is even more difficult to come to a conclusion of the best fitting range with only two sets of experimental data. A way around this difficulty is to compare the CEF calculations to additional experimental data like specific heat and neutron spectra. Hence, rather than having only some experimental data well reproduced, the best fitting range is that which gives CEF calculations that modestly describe all the experimental data: inverse susceptibility, magnetization, specific heat, and neutron spectra.

Chapter 4

Results and Discussion

In Chapters 2 and 3, the CEF theoretical framework and its numerical implementation are introduced and explained with representative examples. In this chapter, the magnetic properties of $CeCd_3X_3$ (X = P and As) under the influence of CEF effects are presented as the main results of the thesis work. A strong easy plane magnetic anisotropy has been observed in $CeCd_3X_3$ compounds. Our analysis of their magnetic susceptibility, magnetization, and specific heat data showed that the observed anisotropy can be explained by a CEF model with Ce^{3+} ions in trigonal symmetry. In particular, the reliability of our CEF analysis on $CeCd_3As_3$ is accessed by comparing with the CEF analyses of earlier reports.

4.1 Physical properties of $CeCd_3X_3$

Geometrically frustrated insulating magnets with $4f$ electrons provide opportunities to study unconventional order parameters such as spin liquid states [48–54]. When $4f$ electrons are located in triangular lattices (TL), spin-orbit coupling enhances quantum fluctuations and promotes nonlocal excitations without magnetic ordering characterized by highly anisotropic interactions between $4f$ moments [55–60]. Several f-electron materials with TL structures have shown rich phenomena. A spin liquid state has been proposed in insulating $YbMgGaO_4$ [5, 61–64] and $NaYbS_2$ [65, 66]. The low carrier density system $YbAl_3C_3$ shows a gap in the magnetic excitation spectrum due to the dimerization of the f electrons in Yb^{3+} pairs [67–70]. In particular, the easy-plane antiferromagnets $CeCd_3X_3$ (X = P and As) have been recently discovered as a new class of TL system, with a low antiferromagnetic ordering temperature and extremely low carrier density [71–75].

The family of compounds with the formula CeM_3X_3 (M = Al, Cd, and Zn and X = C, P, and As) have been investigated for their robust ground state properties arising from the interplay between a geometrically frustrated lattice, CEF, and magnetic exchange interactions [69, 71–77]. These compounds show a very large magnetic anisotropy due to the strong CEF acting on Ce^{3+} ions. $CeCd_3X_3$ materials adopt the hexagonal $ScAl_3C_3$-type structure (space group $P6_3/mmc$) with the Ce atoms having trigonal (D_{3d}) point

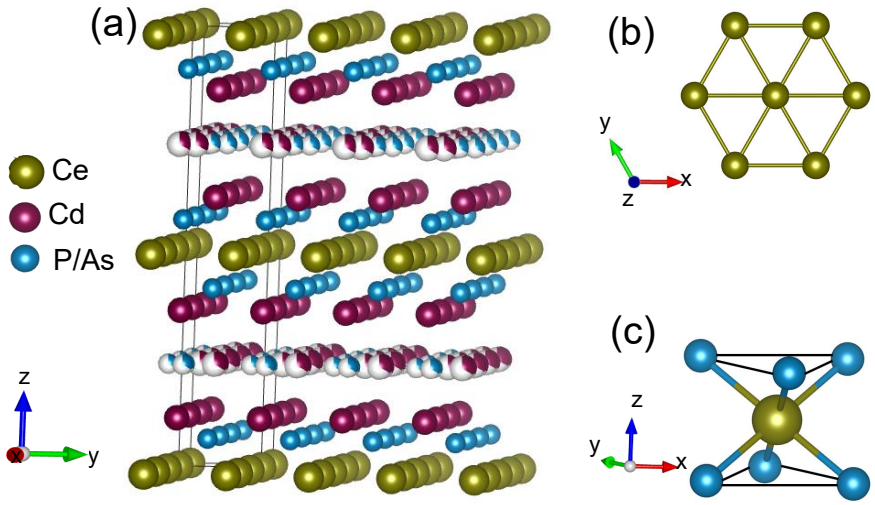

Figure 4.1: Schematic of crystal structure of $CeCd_3X_3$ (X = P, As) in the hexagonal $ScAl_3C_3$-type structure ($P6_3/mmc$, 194) (a) 2D-layered structure showing the crystal unit cell with the atomic positions, Ce atoms are located in the $2a$ Wyckoff position. (b) Ce atoms forming two-dimensional triangular lattices. (c) Ce atom in a trigonal (D_{3d}) point symmetry surrounded by P/As atoms.

symmetry [73–76]. In this crystal structure, the Ce layers are well separated by the Cd and X atoms, forming a layered 2D triangular lattice (TL) in the ab-plane [73–76] as depicted in Fig. 4.1. From thermodynamic and transport property measurements, $CeCd_3X_3$ have been characterized as extremely low-carrier-density metallic systems, with strong easy-plane magnetic anisotropy and antiferromagnetic ordering below T_N ~0.42 K [72, 75]. As temperature decreases, C_m significantly increases below 10 K and indicates a λ-like peak at 0.42 K, a signature of antiferromagnetic ordering. At the magnetic ordering temperature, roughly 40% of $R\ln(2)$ entropy is recovered, implying a doublet ground state resulting from CEF splitting of localized Ce ion energy levels. The highly enhanced specific heat below 10 K and the reduced magnetic entropy at T_N are reminiscent of Kondo lattice materials. However, the electrical resistivity of $CeCd_3X_3$ shows no maximum or logarithmic upturns resulting from the Kondo scattering of conduction electrons from magnetic Ce^{3+} moments, where the resistivity of $CeCd_3X_3$ is the same as that of $LaCd_3X_3$. Therefore, the Kondo screening may not be responsible for these observations. We expect that an absence of Kondo screening in these materials is due to the low carrier density: there are simply not enough carriers to screen the f-electron moments.

In the present study, we use the CEF scheme to clarify the anisotropic magnetic properties of $CeCd_3X_3$. For $CeCd_3As_3$, two independent CEF analyses [46, 73] showed some discrepancies in their studies, by way of inconsistent energy level splittings and different first excited state wave functions. Unlike $CeCd_3As_3$, no CEF analysis has been carried out

for $CeCd_3P_3$. Therefore, this thesis is motivated by the unclear conclusion of the CEF profile of $CeCd_3As_3$ and a lack of the CEF analysis on $CeCd_3P_3$. At high temperatures, the magnetization and specific heat measurements of these compounds can be well explained by the CEF effects, while further studies are necessary to understand low temperature magnetism with a CEF-derived Kramers doublet ground state.

4.2 Determination of CEF parameters

The CEF Hamiltonian, based on the point charge model, assumes that the magnetic ions are well localized with a stable valence state. The valence state of $CeCd_3X_3$ can be deduced from the effective moment of Ce^{3+} ions. Figures 4.2 (a) and (b) show the inverse magnetic susceptibility, $\chi^{-1} = H/M$, curves of $CeCd_3P_3$ and $CeCd_3As_3$, respectively, together with their polycrystalline averages ($\chi_{poly} = 2/3\chi_{ab} + 1/3\chi_c$). At sufficiently high temperatures, magnetic susceptibility curves follow the Curie-Weiss (CW) behavior: $\chi(T) = C/(T - \theta_p)$, where C is the Curie constant and θ_p is Curie-Weiss temperature. For $H \parallel c$ (magnetic hard axis) $\chi(T)$ barely follows the CW law above ~300 K and shows a broad maximum around ~150 K, implying large CEF energy level splittings. By applying the CW law to the polycrystalline averaged curves, the effective moments of $CeCd_3P_3$ and $CeCd_3As_3$ are estimated to be $\mu_{eff} = 2.51\ \mu_B$ and $\mu_{eff} = 2.54\ \mu_B$, respectively, which agree very well with the value $\mu_{eff} = 2.54\ \mu_B$ of free Ce^{3+} ion. From the effective moment values, it is reasonable to assume that Ce ions in these compounds are well localized with 3+ valence state.

For $CeCd_3X_3$ systems, the Ce atoms occupy the $2a$ Wyckoff position and has a trigonal symmetry, as depicted in Fig. 4.1(c). In this configuration, the CEF Hamiltonian requires

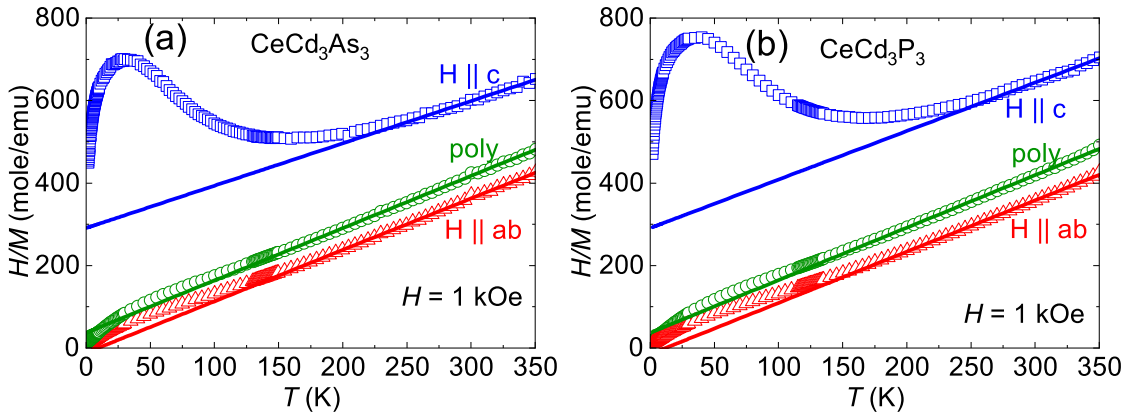

Figure 4.2: (a) $CeCd_3A_3$ inverse magnetic susceptibility $\chi^{-1}(T)$ at 1 kOe for H || ab, H || c, and polycrystalline average. (b) $CeCd_3P_3$ inverse magnetic susceptibility $\chi^{-1}(T)$ at 1 kOe for H || ab, H || c, and polycrystalline average. Solid lines are from the fits of the Curie-Weiss law to the data.

only three parameters [78, 79]: B_2^0, B_4^0, B_4^3 (see Table 2.3). Note that thermodynamic and transport measurements of these compounds indicate a possible structural phase transition below 200 K [69, 72, 75], thus requiring additional CEF parameters below this transition temperature to account for the change in the local environment of the Ce atoms. However, the effect of structural distortion is negligible in the the magnetic susceptibility curves, which shows a smooth evolution through the structural phase transition temperature. Therefore, in our CEF analysis, the trigonal symmetry of the Ce atoms is still used below the phase transition temperature.

As presented in Eqn. 2.24 the B_2^0 parameter gives a measure of the magnetocrystalline anisotropy and can be expressed in terms of the paramagnetic Weiss temperatures [37, 46]. From the Curie-Weiss fit (see Fig.4.2), anisotropic Weiss temperatures of $CeCd_3As_3$ are estimated to be $\theta_{ab} = 9.3$ K and $\theta_c = -283$ K. For $CeCd_3P_3$, $\theta_{ab} = 9.3$ K and $\theta_c = -248$ K are obtained. We can now use these values to estimate the leading CEF parameters, $B_2^0 = 30.48$ K for $CeCd_3As_3$ and $B_2^0 = 26.75$ K for $CeCd_3P_3$, as a starting point for evaluating the CEF scheme.

4.3 CEF scheme of $CeCd_3As_3$

For $CeCd_3As_3$ the CEF parameters and energy profile are summarized respectively in Table 4.1 and Fig. 4.3. As shown in Fig. 4.3 the $2J + 1$ degenerate levels for $J = 5/2$ of Ce^{3+} split into three Kramers doublets with energy level splittings $\Delta_1 = 242$ K and $\Delta_2 = 553$ K. The ground state and second excited state are in an admixture of $|\pm 5/2\rangle$ and $|\mp 1/2\rangle$ states. However, the first excited state is a pure $|\pm 3/2\rangle$ state.

Table 4.1: $CeCd_3As_3$: Comparing the CEF parameters of three studies

	Present study[a]	Ref. [73][b]	Ref. [46][c]
CEF parameters (K):			
B_2^0	18.55	11.50	11.60
B_4^0	-0.08	-1.40	-0.50
B_4^3	23.02	12.00	8.00

[a]Exchange interaction is based on molecular field: $\lambda_{ab} = -5.7$ mole/emu and $\lambda_c = 1.0$ mole/emu

[b]Exchange interaction is based on nearest neighbour spin Hamiltonian see Ref. [73]

[c]Exchange interaction was not considered

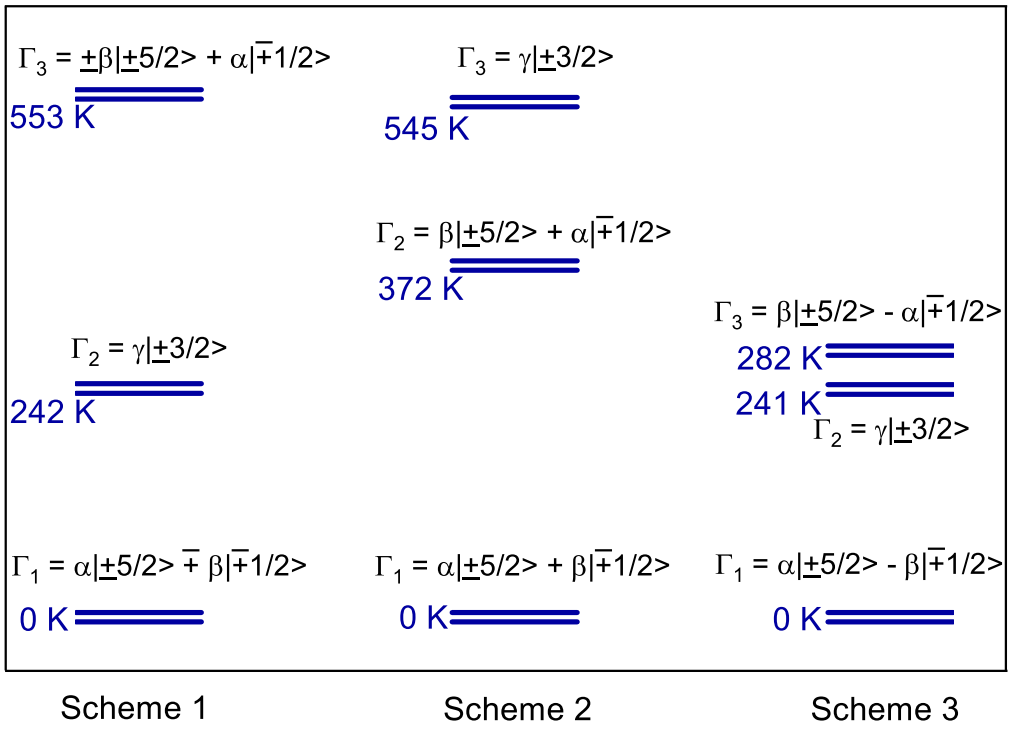

Figure 4.3: Comparison of the CEF energy level splitting and eigenstate of $CeCd_3As_3$ for three different schemes/studies. Scheme 1 is from this present work, with the coefficients of the eigenstates given as $\alpha = 0.44$, $\beta = 0.90$, $\gamma = -1$. Scheme 2 is from Ref. [73], with $\alpha = 0.32$, $\beta = 0.95$, $\gamma = 1$. Scheme 3 is from Ref. [46], with $\alpha = 0.28$, $\beta = 0.96$, $\gamma = 1$.

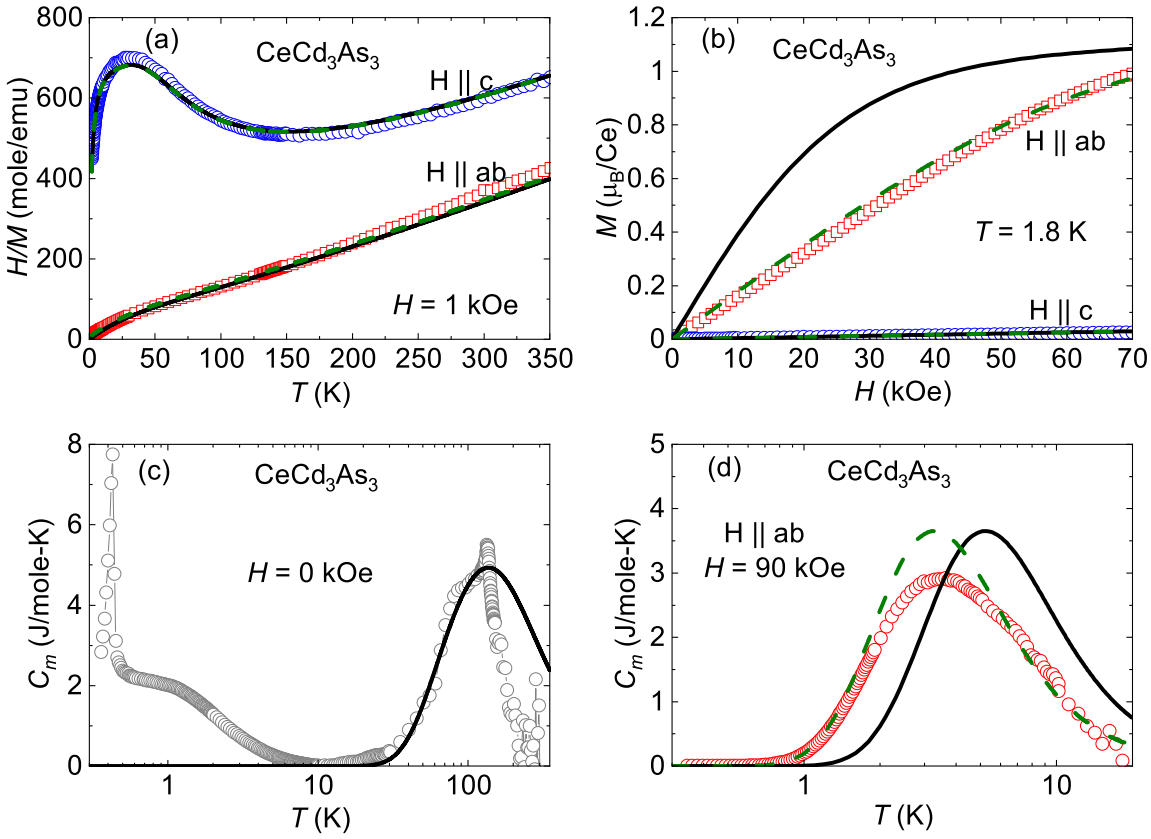

Figure 4.4: $CeCd_3As_3$ magnetic properties and CEF fits. Open symbols are from experimental measurements. Solid lines represent the CEF fit with no molecular field contribution. Dashed lines are CEF fit with molecular field ($\lambda_{ab} = -5.7$ mole/emu, $\lambda_c = 1.0$ mole/emu). (a) Inverse magnetic susceptibility at a field of 1 kOe. (b) Isothermal magnetization as a function of field at 1.8 K. (c) Magnetic specific heat at zero field. (d) Magnetic specific heat at a field of 90 kOe along $H \parallel ab$.

Figure 4.4 displays the anisotropic magnetic susceptibility curves, magnetization isotherms, and specific heat of $CeCd_3As_3$, together with the CEF calculations. At first, without molecular field contributions, we discuss the CEF effects on the thermodynamic properties of $CeCd_3As_3$. In Fig. 4.4 (a), solid lines represent the CEF fit to the magnetic susceptibility data with $\lambda_i = 0$. The CEF fit generally agrees with the inverse magnetic susceptibility, as the large anisotropy between crystallographic directions is captured. Although a tiny misalignment is seen for the temperature range between 225 K and 350 K, a good fit is obtained for measurements below 220 K. For $H \parallel ab$, the broad hump around 25 K is well reproduced. The CEF model aligns very well with the magnetization isotherm, $M(H)$, for $H \parallel c$ at 1.8 K, whereas there is an inconsistency between the CEF calculation and $M(H)$ for $H \parallel ab$, as shown in Fig. 4.4 (b). C_m at $H = 0$ and 90 kOe is presented in Figs. 4.4 (c) and (d), respectively. In zero field, the broad maximum around 100 K from the Schottky contribution is roughly reproduced by the CEF model. Note that the additional peak around 130 K is an anomaly attributed to a structural phase transition, as discussed in Ref. [72]. The C_m below the peak is well captured by the CEF calculation, but the CEF calculation is not consistent with the experimental data above the peak. This inconsistency at high temperatures is caused by the very large subtraction error in calculating C_m ($= C_p[CeCd_3As_3] - C_p[LaCd_3As_3]$), as explained in Ref. [72]. The sharp rise of C_m below 10 K and the sharp peak at $T_N = 0.42$ K [72] are not captured by the CEF model. The origin of these low temperature behaviors is suggested to be due to the combination of magnetic frustration and antiferromagnetic ordering [72]. At $H = 90$ kOe for $H \parallel ab$, the overall shape of the C_m is captured by the CEF model, but the maximum temperature is higher than that of experimental data.

The CEF model without λ_i does not adequately reproduce $M(H)$ and C_m data for $H \parallel ab$. In order to account for the mismatch, the molecular field interactions between Ce^{3+} ions are incorporated (see the Sec. 3.1.3 in Chapter 3). The dashed-lines in Fig. 4.4 represent the CEF model in the presence of the molecular field terms $\lambda_{ab} = -5.7$ mole/emu and $\lambda_c = 1$ mole/emu. By introducing the molecular terms, the magnetic susceptibility curves show a slightly better agreement of the CEF calculation to the experimental data at high temperatures. However, as can be clearly seen, the $M(H)$ curve for $H \parallel ab$ is captured by the combination of the CEF scheme and molecular field interactions. Moreover, although the absolute value of the maximum in C_m at 90 kOe is slightly higher, the position of the maximum temperature is well reproduced by the CEF model (Fig. 4.4(c)). These results point to the importance of including the exchange interactions between Ce^{3+} magnetic ions.

Since the CEF analysis of $CeCd_3As_3$ has been reported in Refs. [46, 73], the present work on $CeCd_3As_3$ is compared with the CEF results from earlier studies [46,73]. The CEF parameters are summarized in Table 4.1. The energy level splittings, and corresponding eigenstates are shown in Fig. 4.3.

In Fig. 4.3, for all 3 schemes, the ground state is in a mixed states of $|\pm 5/2\rangle$ and $|\mp 1/2\rangle$ with a higher probability in the $|\mp 1/2\rangle$ state. This requires a mixing angle θ in the wave function: $\cos(\theta)|\pm 5/2\rangle + \sin(\theta)|\mp 1/2\rangle$. The obtained mixing angle is roughly similar for all three studies: 64° in this study, 72° in Ref. [73], and 74° in Ref. [46]. Unlike the ground state that is the same for all 3 studies, the excited states $|\Gamma_2\rangle$ and $|\Gamma_3\rangle$ do not entirely agree for all 3 reports. The $|\Gamma_2\rangle$ and $|\Gamma_3\rangle$ excited states for this study and that of Ref. [46] are consistent. That is, the $|\Gamma_2\rangle$ excited state is in a pure state of $|\pm 3/2\rangle$ and the $|\Gamma_3\rangle$ excited state is in a mixed state of $|\pm 5/2\rangle$ and $|\mp 1/2\rangle$. However, in Ref. [73] there is a clear swap of these excited state wave functions. This disagreement between the excited states of Ref. [73] and the two other reports, is suggested to be due to their relative higher magnitude of $|B_4^0|$. (As shown in Table 4.1 $|B_4^0| = 1.4$ K for Ref. [73], this is larger than $|B_4^0|$ value of 0.08 K and 0.5 K of this present work and that of Ref. [46] respectively). In fact, we confirmed that any $|B_4^0| > 0.7$ K would result in the $|\Gamma_2\rangle$ being in a mixed state and the $|\Gamma_3\rangle$ being in a pure state, just as the case of Ref. [73]. Another important distinction among these 3 studies is in the energy level splitting presented in Fig. 4.3. The energy level splitting from the ground to the first excited state is comparable for all studies. However, the energy eigenvalue for the second excited state indicates a discrepancy, where the value in Ref. [46] is roughly two times smaller than that of the other two studies.

Using the CEF parameters presented in Table 4.1, $\chi^{-1}(T)$ and $M(H)$ curves for three studies are compared and plotted in Fig. 4.5. The plots from this study (Fig. 4.5(a) and (b)) are calculated by including the the molecular field contribution. Fig. 4.5(c) and (d) are the results taken from Ref. [73], where the CEF scheme is obtained in the present of an antiferromagnetic exchange interaction based on a mean-field approach [73, 80]. Lastly, solid lines in Figs. 4.5(e) and (f), taken from Ref. [46], represent the CEF calculations, where the CEF parameters are obtained by fitting the magnetic susceptibility curves to only CEF Hamiltonian (no exchange interaction term was included). As can be seen from the plots, the calculated $\chi^{-1}(T)$ curves for all three studies are similar, especially that they capture the broad hump in the curves for $H \parallel c$. It has to be noted that the CEF calculation in Ref. [73] shows a significant deviation from the experimental data, which was reported to be due to the measurement errors arising from the very small sample size [73]. In addition, the minor difference in experimental magnetic susceptibility curves is mainly due to the different sample quality. The large magnetic anisotropy in $M(H)$ curves can be well described by CEF models for all three studies. However, the CEF model with exchange interactions gives a better description of experimental data, implying the importance of the exchange interaction in $CeCd_3As_3$.

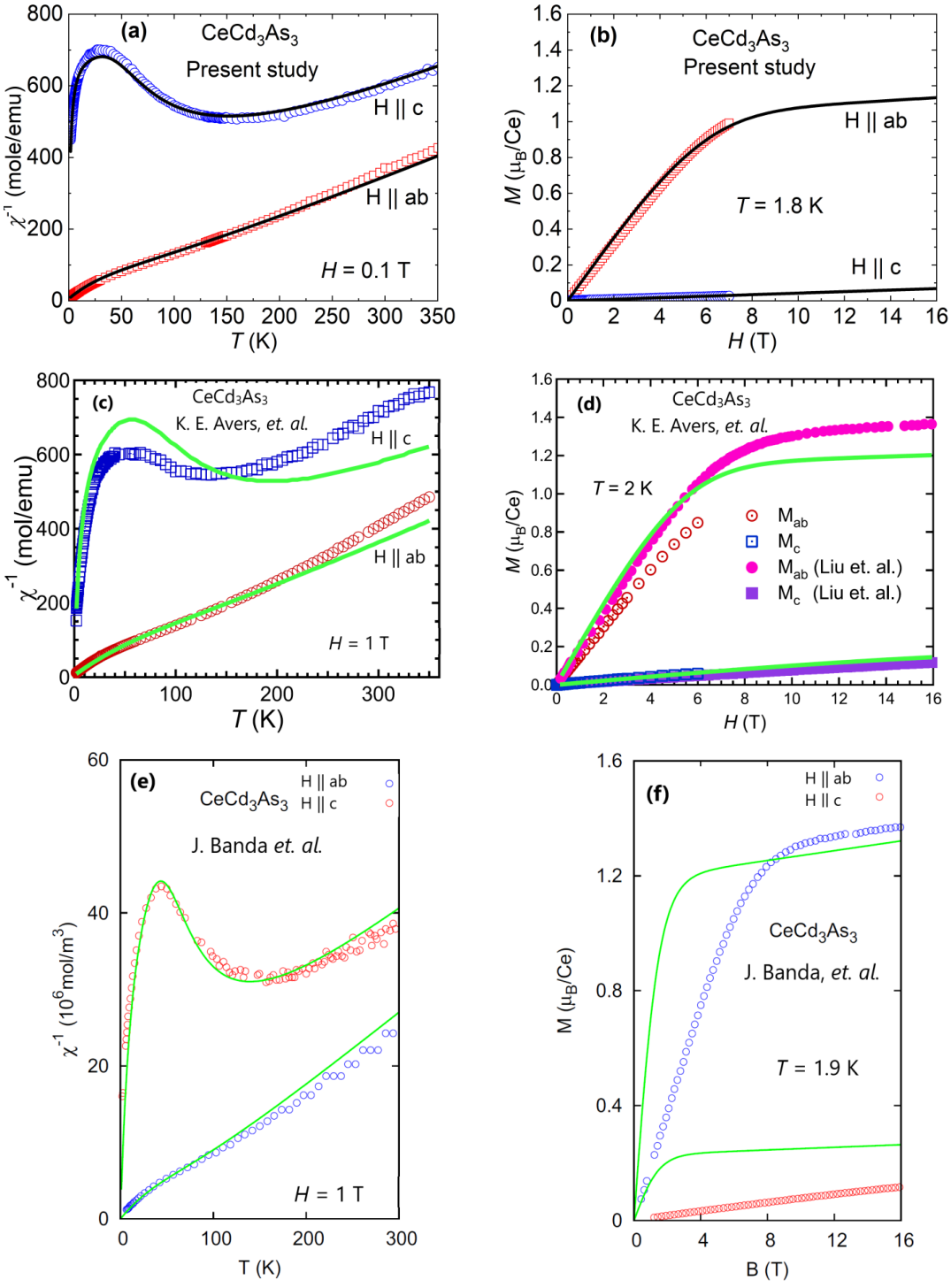

Figure 4.5: (a) $\chi^{-1}(T)$ of this present study. (b) $M(H)$ of this present study. (c) $\chi^{-1}(T)$ of Ref. [73]. (d) $M(H)$ of Ref. [73].(e) $\chi^{-1}(T)$ of Ref. [46]. (f) $M(H)$ of Ref. [46]. In all plots open/solid symbols are measurement data whereas solid lines are CEF calculations. Note that, K. E. Avers, *et al.* reported two data types. The open symbols are from their own measurements upto 7 T fields Ref. [73], whereas the solid symbols are data gotten from Ref. [71].

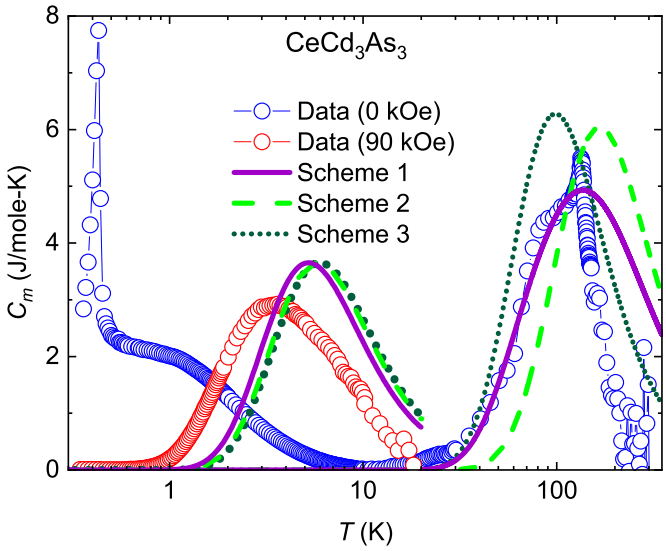

Figure 4.6: Comparison of the CEF-derived C_m between the 3 studies. Solid lines are from this present study (Scheme 1), dashed lines are from Ref. [73] (Scheme 2), and dotted lines are from Ref. [46] (Scheme 3). Open symbols are from our experimental measurements. Field is along $H \parallel ab$. Note that molecular field contribution is not taken into account for 90 kOe data.

Figure 4.6 shows the magnetic part of the specific heat, calculated by the CEF parameters for all three schemes/studies. The open symbols represent experimental data from this study. Solid lines, dashed lines, and dotted lines are CEF calculations from the present study, Ref. [73] and Ref. [46], respectively. As shown in the figure, when subtle differences are ignored, the high temperature maximum is captured by all three calculated curves. This implies that the high temperature maximum in C_m is due to the CEF effects and the ground state doublet is well isolated from the first and second excited states. When the measurement uncertainty and different sample quality are considered, the best CEF parameters among three CEF parameter sets cannot be selected from the comparison of specific heat. Therefore, further measurements such as inelastic neutron scattering are necessary to distinctly specify the best CEF model in this system. Nevertheless, it is clear from the CEF analysis that the large enhancement of C_m below 10 K cannot be explained by the Schottky contribution.

4.4 CEF scheme of $CeCd_3P_3$

We now turn to the CEF analysis for $CeCd_3P_3$, following the same procedure applied to $CeCd_3As_3$. The isostructural compounds $CeCd_3P_3$ and $CeCd_3As_3$ show remarkably similar magnetic properties, implying that their local CEF environments are in close resemblance.

Table 4.2: $CeCd_3P_3$: CEF parameters, Eigenvectors and Eigenvalues

CEF parameters						
	B_2^0 (K)	B_4^0 (K)	B_4^3 (K)	λ_i (mole/emu)		
	20.90	-0.03	26.00	$\lambda_{ab} = -6.2$, $\lambda_c = 0.3$		
Energy levels and states						
E (K)	$\|-\frac{5}{2}\rangle$	$\|-\frac{3}{2}\rangle$	$\|-\frac{1}{2}\rangle$	$\|\frac{1}{2}\rangle$	$\|\frac{3}{2}\rangle$	$\|\frac{5}{2}\rangle$
0	0.0	0.0	$\mp$0.897	0.0	0.0	0.442
0	0.442	0.0	0.0	$\pm$0.897	0.0	0.0
257	0.0	-1.0	0.0	0.0	0.0	0.0
257	0.0	0.0	0.0	0.0	-1.0	0.0
621	-0.897	0.0	0.0	$\pm$0.442	0.0	0.0
621	0.0	0.0	$\pm$0.442	0.0	0.0	0.897

Hence, it is expected that the CEF parameters will be quite similar for both compounds, giving rise to very similar CEF energy level splittings and eigenstates.

Table 4.2 shows a summary of CEF fit results of $CeCd_3P_3$. As expected, the obtained CEF parameters, eigenstates, and eigenvalues for $CeCd_3P_3$ are very similar to the case for $CeCd_3As_3$ (see Table 4.1 and Fig. 4.3). The positive B_2^0 term indicates that the magnetization lies in easy plane as seen in Fig. 4.7(b). The large B_4^3 term implies a mixed ground state with $|\pm 5/2\rangle$ and $|\pm 1/2\rangle$, just like the case for $CeCd_3A_3$. The first excited state is in a pure state of $|\pm 3/2\rangle$ and the second excited state is in an admixture of $|\pm 5/2\rangle$ and $|\pm 1/2\rangle$ states. The energy level splittings correspond to 257 K for the first excited state and 621 K for the second excited state.

Figure 4.7 shows the magnetic susceptibility, magnetization, and specific heat curves together with the CEF calculations. In the absence of molecular field terms, the CEF calculations (solid lines) agree very well with the experimental H/M curves, as shown in Fig. 4.7 (a). Notably, as with the case for $CeCd_3As_3$, the CEF model captures the broad hump around 30 K. Also, C_m in zero field agrees with the CEF fit at high temperatures, as shown in Fig. 4.7(c), implying the high temperature broad maximum (Schottky anomaly) is due to the CEF effects. However, the CEF calculation does not align with the $M(H)$ curve for $H \parallel ab$ at 1.8 K, displaying the same characteristic with that of $CeCd_3As_3$. In addition, the CEF calculation does not agree with the experimental C_m data at $H = 90$ kOe as it appears to shift rightwards. This indicates that in addition to the Zeeman effect other contribution must be considered.

In order to capture the experimental data in a better way, the molecular field terms are added into the Hamiltonian and the results are plotted in Fig. 4.7 (dashed lines). Although the calculation of magnetic susceptibility is hardly affected (almost no change), the inclusion of the molecular field terms greatly alters the $M(H)$ curve calculation for $H \parallel ab$ and adequately captures the experimental $M(H)$ behavior as as shown in Fig. 4.7(b). In addition,

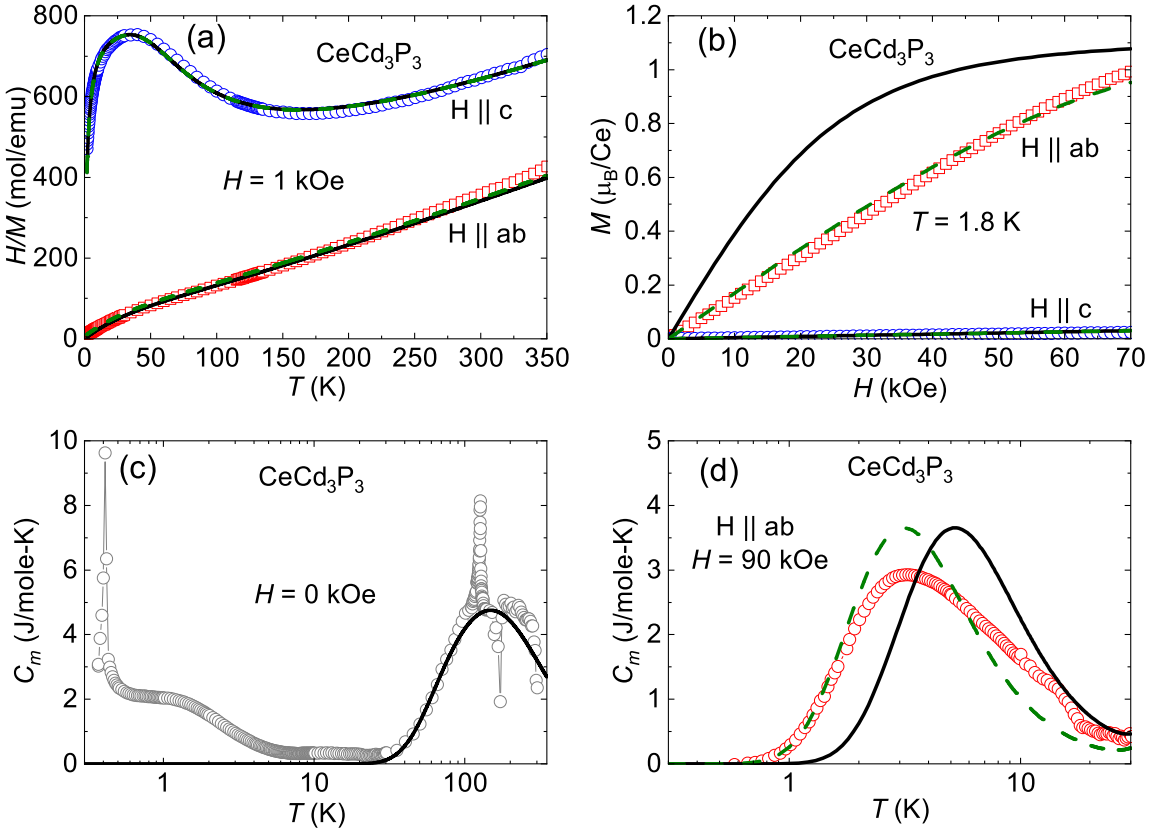

Figure 4.7: $CeCd_3P_3$ magnetic properties and CEF fits. Open symbols are from experimental measurements. Solid lines represent the CEF fit with no molecular field contribution. Dashed lines are CEF fit with molecular field ($\lambda_{ab} = -6.3$ mole/emu, $\lambda_c = 0.3$ mole/emu). (a) Inverse magnetic susceptibility at a field of 1 kOe. (b) Isothermal magnetization as a function of field at 1.8 K. (c) Magnetic specific heat at zero field. (d) Magnetic specific heat at a field of 90 kOe along $H \parallel ab$

the CEF calculation with molecular field terms properly captures the low temperature maximum in C_m at $H = 90$ kOe (see Fig. 4.7(c)). Therefore, we conclude that the CEF model in the present of the molecular field interaction should be used to describe the experimental data for $CeCd_3P_3$. As expected from the layered crystal structure, the absolute value of λ_{ab} is greater than λ_c, implying a strong exchange interaction in the ab-plane.

The obtained values of CEF parameters of $CeCd_3P_3$ are slightly larger than those of $CeCd_3As_3$. The slight difference in the values of their CEF parameters is quite surprising. When the distance between Ce^{3+} and nearest P/As atoms is considered, the difference between Ce-As distance (3.05 Å) and Ce-P distance (2.96 Å) is about ∼9 pm, which may not be large enough to lead to quite different CEF energy level splittings [72, 73, 75].

4.5 CEF in other Ce-based trigonal systems

The significance of B_4^3 CEF parameter has been observed in Ce-based antiferromagnets such as CeAuSn, $CeIr_3Ge_7$, $CePtAl_4Ge_2$, $CeCd_3As_3$ and $CeCd_3P_3$, where Ce ions are in a local trigonal environment [46, 78, 79, 81]. These compounds indicate a huge magnetic anisotropy with the ab-plane being the magnetic easy plane, which can be qualitatively explained by CEF effects. In addition, a relatively low magnetic ordering temperature is observed in this family of materials.

A detailed CEF analysis based on both the magnetic susceptibility and inelastic neutron scattering data of hexagonal CeAuSn indicates a mixture of the $|\pm 5/2\rangle$ and $|\mp 1/2\rangle$ CEF ground state doublet, a pure $|\pm 3/2\rangle$ doublet as the first excited state, and a mixture of the $|\pm 5/2\rangle$ and $|\mp 1/2\rangle$ as the second excited doublet state, with energy level splitting of ∼345 K and ∼440 K [78, 81]. The obtained CEF parameters from the analysis of magnetic susceptibility and neutron scattering are $B_2^0 = 16.21$ K, $B_4^0 = -0.64$ K, and $B_4^3 = 15.32$ K [81] and $B_2^0 = 11.01$ K, $B_4^0 = -0.58$ K, and $B_4^3 = 19.66$ K [78], respectively. Both analyses clearly show a significant B_4^3 contribution corresponding to a large mixing angle, consistent with CEF analysis of $CeCd_3As_3$ and $CeCd_3P_3$.

The CEF investigation of the rhombohedral $CeIr_3Ge_7$ compound shows very similar CEF eigenstates and eigenvalues with those of other compounds. However, in $CeIr_3Ge_7$, the reported CEF parameters ($B_2^0 = 34.4$ K, $B_4^0 = -0.82$ K, $B_4^3 = 67.3$ K) are slightly larger than that of other compounds, inducing a huge energy level splittings of 374 K and 1398 K [46]. It has been suggested that the exceptionally large CEF splitting can be related to the contribution of $5d$ ligands of Ir atoms [46].

In addition, the CEF analysis on rhombohedral $CePtAl_4Ge_2$ antiferromagnet has also been conducted [79]. Unlike the above mentioned compounds, the ground state and the second excited state of $CePtAl_4Ge_2$ are not in a mixed configuration of $|5/2\rangle$ and $|1/2\rangle$ states. The sign and magnitude of B_2^0 (= 13.26 K) and B_4^0 (= −0.3 K) CEF parameters in $CePtAl_4Ge_2$ are comparable to that of CeAuSn, $CeIr_3Ge_7$, and $CeCd_3X_3$ (X = P and As).

However, because the B_4^3 term responsible for mixing is exceptionally small in $CePtAl_4Ge_2$ system ($B_4^3 = 0 \pm 0.02$ K), the ground state and second excited state is in a pure $|\pm 1/2\rangle$ state and a pure $|\mp 5/2\rangle$ state, respectively. The small value of B_4^3 term implies a relatively smaller magnetic anisotropy in $CePtAl_4Ge_2$, which is clearly reflected on its magnetic susceptibility data [79].

4.6 Summary and outlook

At high temperatures, the observed physical properties of $CeCd_3X_3$ compounds can be understood by considering the CEF effects. When the temperature becomes comparable to the CEF splitting, excited CEF levels get thermally populated and become relevant. It is clear from the CEF analysis that the large anisotropy in the magnetic susceptibility and magnetization, and the high temperature electronic Schottky anomaly in the specific heat are explained by energy level splittings of the $J = 5/2$ Hund's rule ground state of Ce^{3+} ions into three doublets. Note that the validity of the CEF Hamiltonian must be verified below the (structural) phase transition temperature $T_s = 127$ K for $CeCd_3P_3$ [75] and $T_s = 136$ K for $CeCd_3As_3$ [72]. In addition, inelastic neutron scattering experiments are required to resolve the discrepancies among the three independent CEF analyses for $CeCd_3As_3$.

Although our CEF analysis on $CeCd_3X_3$ compounds provides a comprehensive picture at high temperatures, a number of unanswered questions remain at low temperatures. When the temperature is much lower than the CEF splitting, the lowest Kramers doublet is only relevant to explain the observed magnetic ordering at $T_N = 0.42$ K and the upturn in C_m below 10 K. It is obvious that the temperature dependence and absolute value of C_m below 10 K cannot be explained by the electronic Schottky contribution (see Figs. 4.4 (c) and 4.7 (c)). Since magnetization isotherms at $T = 1.8$ K for both compounds are mostly reproduced by CEF calculation with the ground state wave function, the reduction of the magnetization is due to the CEF effect, implying that the Kondo screening in both compounds is negligible. This is consistent with the electrical resistivity results of $CeCd_3X_3$. Hence, as suggested in Refs. [72, 75], the enhancement of the specific heat below 10 K is probably related to either the magnetic frustration in triangular lattices [71–75] or simply the magnetic fluctuations observed in insulating antiferromagnets [82].

The transport property measurements of $CeCd_3X_3$ suggest that an RKKY interaction may be responsible for the magnetic ordering. However, it would have to be mediated by a small number of conduction electrons, given the remarkably high resistivity value and low carrier density of these compounds. It has been suggested that the superexchange interaction in low carrier density $YbAl_3C_3$ compound becomes dominant instead of the RKKY interaction, where the carrier concentration is estimated to be $n \sim 0.01$ per formula unit [67]. When the carrier concentrations of $CeCd_3As_3$ ($n \sim 0.003$ per formula unit) [72] and $CeCd_3P_3$ ($n \sim 0.002$ per formula unit) [75] compounds are considered, it is not unreasonable to assume

that the superexchange interaction may be responsible for the antiferromagnetic ordering below 0.42 K. The partial $H - T$ phase diagram of these compounds, especially the field-induced increase of T_N, is also similar to that of 2D insulating triangular lattice systems with easy-plane anisotropy [54, 83]. In addition, the low temperature specific heat results of $CeCd_3As_3$, grown by chemical vapor transport (CVT), can be explained by anisotropic exchange Hamiltonian for an insulating, layered triangular lattice [73]. Note that the flux-grown $CeCd_3As_3$ [72] shows a metallic behavior, whereas the CVT grown $CeCd_3As_3$ [73] indicates a semiconducting behavior. However, except for the resistivity, there are no noticeable differences between these samples in terms of magnetization and specific heat. For $CeCd_3X_3$, the field-induced increase of T_N and extremely low carrier density suggest the superexchange mechanism for the magnetic ordering, where the lowest Kramers doublet is responsible for the dominant magnetic properties.

Chapter 5

Conclusion

In summary, the *PyCrystalField* CEF program has been modified to improve CEF fitting by way of incorporating exchange interaction via the molecular field approximation. Using this modified CEF program a set of fitted CEF parameters were obtained for $CeCd_3As_3$ and $CeCd_3P_3$ and their physical properties were analyzed. The fitted CEF parameters are $B_2^0 = 18.55$ K, $B_4^0 = -0.08$ K, $B_4^3 = 23.02$ K for $CeCd_3As_3$ with energy level splittings of 242 K and 553 K. Those of $CeCd_3P_3$ are $B_2^0 = 20.90$ K, $B_4^0 = -0.03$ K, $B_4^3 = 26.00$ K, with energy level splittings of 257 K and 621 K. The large B_4^3 values of both compounds give a ground state which is mixture of $|\pm 5/2\rangle$ and $|\mp 1/2\rangle$ states, with a dominant $|\mp 1/2\rangle$ character. The magnetic susceptibility data matches the CEF calculations of both $CeCd_3As_3$ and $CeCd_3P_3$. The isothermal magnetization curves at 1.8 K are readily reproduced when the exchange interaction terms are added to the Hamiltonian. For both compounds, the broad maximum in the magnetic specific heat is well explained by the Schottky anomaly. At high temperatures, our CEF analysis provides a satisfactory description of the magnetic properties of $CeCd_3As_3$ and $CeCd_3P_3$, where the striking similarity of the CEF profile of both compounds implies a very close resemblance of their crystal field environment. At low temperatures, further measurements such as magnetization, nuclear magnetic resonance (NMR), and neutron scattering are necessary to provide further insight into the nature of magnetism below T_N and the role of anisotropic exchange interactions in the triangular motif. Furthermore, our CEF analysis on $CeCd_3As_3$ is compared to those of two earlier studies. Such comparison of the three studies shows inconsistent CEF energy levels and eigenstates, requiring further studies.

Bibliography

[1] G. Busch, *Magnetic Properties of Rare-Earth Compounds*, Journal of Applied Physics **38**, 1386 (1967).

[2] T. T. M. Palstra, G. Lu, A. A. Menovsky, G. J. Nieuwenhuys, P. H. Kes, and J. A. Mydosh, *Superconductivity in the ternary rare-earth (Y, La, and Lu) compounds* $R\mathrm{Pd}_2\mathrm{Si}_2$ *and* $R\mathrm{Rh}_2\mathrm{Si}_2$, Phys. Rev. B **34**, 4566 (1986).

[3] K. H. J. Buschow and H. J. van Daal, *Evidence for the Presence of the Kondo effect in the Compound* $Ce\mathrm{Al}_2$, Phys. Rev. Lett. **23**, 408 (1969).

[4] P. Lethuillier and P. Haen, *First Observation of a Kondo Effect from Praseodymium Excited Crystal-Field Levels in* $\mathrm{La}_{1-x}\mathrm{Pr}_x\mathrm{Sn}_3$ *Compounds*, Phys. Rev. Lett. **35**, 1391 (1975).

[5] Y. Li, H. Liao, Z. Zhang, S. Li, F. Jin, L. Ling, L. Zhang, Y. Zou, L. Pi, Z. Yang, J. Wang, Z. Wu, and Q. Zhang, *Gapless quantum spin liquid ground state in the two-dimensional spin*$-1/2$ *triangular antiferromagnet* $YbMgGaO_4$, Scientific Reports **5**, 16419 (2015).

[6] W. Liu, Z. Zhang, J. Ji, Y. Liu, J. Li, X. Wang, H. Lei, G. Chen, and Q. Zhang, *Rare-earth chalcogenides: A large family of triangular lattice spin liquid candidates*, Chinese Physics Letters **35**, 117501 (2018).

[7] J. Zhou and G. A. Fiete, *Rare earths in a nutshell*, Physics Today **73**, 66 (2020).

[8] J. M. Coey, *Magnetism and magnetic materials*, Cambridge university press, 2010.

[9] A. Schröder, R. Van den Berg, H. Löhneysen, W. Paul, and H. Lueken, *Magnetic ordering of* $CePt_5$, Solid state communications **65**, 99 (1988).

[10] A. Sumiyama, Y. Oda, H. Nagano, Y. Ōnuki, K. Shibutani, and T. Komatsubara, *Coherent Kondo State in a Dense Kondo Substance:* $Ce_xLa_{1-x}Cu_6$, Journal of the Physical Society of Japan **55**, 1294 (1986).

[11] C. Petrovic, R. Movshovich, M. Jaime, P. Pagliuso, M. Hundley, J. Sarrao, Z. Fisk, and J. Thompson, *A new heavy-fermion superconductor* $CeIrIn_5$*: A relative of the cuprates?*, EPL (Europhysics Letters) **53**, 354 (2001).

[12] R. Sibille, E. Lhotel, V. Pomjakushin, C. Baines, T. Fennell, and M. Kenzelmann, *Candidate quantum spin liquid in the* Ce^{3+} *pyrochlore stannate* $Ce_2Sn_2O_7$, Physical review letters **115**, 097202 (2015).

[13] B. Gao, T. Chen, D. W. Tam, C.-L. Huang, K. Sasmal, D. T. Adroja, F. Ye, H. Cao, G. Sala, M. B. Stone, C. Baines, J. A. T. Verezhak, H. Hu, J.-H. Chung, X. Xu, S.-W. Cheong, M. Nallaiyan, S. Spagna, M. B. Maple, A. H. Nevidomskyy, E. Morosan, G. Chen, and P. Dai, *Experimental signatures of a three-dimensional quantum spin liquid in effective spin-1/2 $Ce_2Zr_2O_7$ pyrochlore*, Nature Physics **15**, 1052 (2019).

[14] F. Steglich, J. Aarts, C. Bredl, W. Lieke, D. Meschede, W. Franz, and H. Schäfer, *Superconductivity in the presence of strong Pauli paramagnetism: $CeCu_2Si_2$*, Physical Review Letters **43**, 1892 (1979).

[15] H. Hegger, C. Petrovic, E. G. Moshopoulou, M. F. Hundley, J. L. Sarrao, Z. Fisk, and J. D. Thompson, *Pressure-Induced Superconductivity in Quasi-2D* $CeRhIn_5$, Phys. Rev. Lett. **84**, 4986 (2000).

[16] C. Tang, Y. Li, J. Du, G. Wu, and W. Zhan, *Effects of rare-earth substitution in $CeFe_2$: mixed-valence and magnetic properties*, Journal of Physics: Condensed Matter **11**, 2027 (1999).

[17] Y. Lai, S. E. Bone, S. Minasian, M. G. Ferrier, J. Lezama-Pacheco, V. Mocko, A. S. Ditter, S. A. Kozimor, G. T. Seidler, W. L. Nelson, Y.-C. Chiu, K. Huang, W. Potter, D. Graf, T. E. Albrecht-Schmitt, and R. E. Baumbach, *Ferromagnetic quantum critical point in* $CePd_2P_2$ *with Pd $\rightarrow$ Ni substitution*, Phys. Rev. B **97**, 224406 (2018).

[18] D. Das, D. Gnida, P. Wiśniewski, and D. Kaczorowski, *Magnetic field-driven quantum criticality in antiferromagnetic $CePtIn_4$*, Proceedings of the National Academy of Sciences **116**, 20333 (2019).

[19] D. Kunwar, R. Adhikari, N. Pouse, M. Maple, M. Dzero, and C. Almasan, *Quantum criticality in $Ce_{1-x}Sm_xCoIn_5$*, Physical Review B **103** (2021).

[20] E. Bauer, *Anomalous properties of Ce-Cu- and Yb-Cu-based compounds*, Advances in Physics **40**, 417 (1991).

[21] E. Bauer and M. Rotter, *Magnetism of complex metallic alloys: Crystalline electric field effects*, pages 183–248.

[22] H. A. Bethe, *Termaufspaltung in Kristallen. (German) [Term splitting in crystals]*, **395**, 133 (1929).

[23] J. H. Van Vleck, *Theory of the Variations in Paramagnetic Anisotropy Among Different Salts of the Iron Group*, Phys. Rev. **41**, 208 (1932).

[24] M. Hutchings, Point-charge calculations of energy levels of magnetic ions in crystalline electric fields, volume 16 of *Solid State Physics*, pages 227 – 273, Academic Press, 1964.

[25] K. W. H. Stevens, *Symmetry and Experiment in Magnetism*, pages 1–7, Springer US, Boston, MA, 1980.

[26] A. Scheie, M. Sanders, J. Krizan, A. D. Christianson, V. O. Garlea, R. J. Cava, and C. Broholm, *Crystal field levels and magnetic anisotropy in the kagome compounds $Nd_3Sb_3Mg_2O_{14}$, $Nd_3Sb_3Zn_2O_{14}$, and $Pr_3Sb_3Mg_2O_{14}$*, Phys. Rev. B **98**, 134401 (2018).

[27] A. Scheie, V. O. Garlea, L. D. Sanjeewa, J. Xing, and A. S. Sefat, *Crystal-field Hamiltonian and anisotropy in $KErSe_2$ and $CsErSe_2$*, Phys. Rev. B **101**, 144432 (2020).

[28] T. Takeuchi, A. Thamizhavel, T. Okubo, M. Yamada, N. Nakamura, T. Yamamoto, Y. Inada, K. Sugiyama, A. Galatanu, E. Yamamoto, K. Kindo, T. Ebihara, and Y. Ōnuki, *Anisotropic, thermal, and magnetic properties of* $CeAgSb_2$ *: Explanation via a crystalline electric field scheme*, Phys. Rev. B **67**, 064403 (2003).

[29] N. Van Hieu, T. Takeuchi, H. Shishido, C. Tonohiro, T. Yamada, H. Nakashima, K. Sugiyama, R. Settai, T. D. Matsuda, Y. Haga, M. Hagiwara, K. Kindo, S. Araki, Y. Nozue, and Y. Ōnuki, *Magnetic Properties and Crystalline Electric Field Scheme in $RRhIn_5$ (R: Rare Earth)*, Journal of the Physical Society of Japan **76**, 064702 (2007).

[30] C. Kittel, *Solid State Physics*, volume 8, Wiley, 2004.

[31] S. Blundell, *Magnetism in Condensed Matter*, OUP Oxford, 2001.

[32] A. J. Freeman and R. E. Watson, *Theoretical Investigation of Some Magnetic and Spectroscopic Properties of Rare-Earth Ions*, Phys. Rev. **127**, 2058 (1962).

[33] W. B. Lewis, J. B. Mann, D. A. Liberman, and D. T. Cromer, *Calculation of Spin–Orbit Coupling Constants and Other Radial Parameters for the Actinide Ions Using Relativistic Wavefunctions*, The Journal of Chemical Physics **53**, 809 (1970).

[34] K. W. H. Stevens, *Matrix Elements and Operator Equivalents Connected with the Magnetic Properties of Rare Earth Ions*, Proceedings of the Physical Society. Section A **65**, 209 (1952).

[35] D. A. Varshalovich, A. N. Moskalev, and V. K. Khersonskii, *Quantum Theory of Angular Momentum*, WORLD SCIENTIFIC, 1988.

[36] Y.-L. Wang, *Crystal-field effects of paramagnetic Curie temperature*, Physics Letters A **35**, 383 (1971).

[37] G. J. Bowden, D. S. P. Bunbury, and M. A. H. McCausland, *Crystal fields and magnetic anisotropy in the molecular field approximation. I. General considerations*, **4**, 1840 (1971).

[38] O. Arnold, J. Bilheux, J. Borreguero, A. Buts, S. Campbell, L. Chapon, M. Doucet, N. Draper, R. Ferraz Leal, M. Gigg, V. Lynch, A. Markvardsen, D. Mikkelson, R. Mikkelson, R. Miller, K. Palmen, P. Parker, G. Passos, T. Perring, P. Peterson, S. Ren, M. Reuter, A. Savici, J. Taylor, R. Taylor, R. Tolchenov, W. Zhou, and J. Zikovsky, *Mantid—Data analysis and visualization package for neutron scattering and μ SR experiments*, Nuclear Instruments and Methods in Physics Research Section A: Accelerators, Spectrometers, Detectors and Associated Equipment **764**, 156 (2014).

[39] M. Rotter, *Using McPhase to calculate magnetic phase diagrams of rare earth compounds*, Journal of Magnetism and Magnetic Materials **272-276**, E481 (2004), http://www.mcphase.de/.

[40] J. J. Baldoví, S. Cardona-Serra, J. M. Clemente-Juan, E. Coronado, A. Gaita-Ariño, and A. Palii, *SIMPRE: A software package to calculate crystal field parameters, energy levels, and magnetic properties on mononuclear lanthanoid complexes based on charge distributions*, Journal of Computational Chemistry **34**, 1961 (2013).

[41] A. T. Boothroyd, *Spectre − a program for calculating spectroscopic properties of rare earth ions in crystals*, (2014), https://xray.physics.ox.ac.uk/software.htm.

[42] R. Osborn, *CFcal*, (2017), https://github.com/rayosborn/cfcal.

[43] P. Fabi, *FOCUS: an interactive crystal electric field parameter fitting package using neutron scattering data*, Council for the Central Laboratory of the Research Councils, 1995.

[44] A. Scheie, *PyCrystalField: software for calculation, analysis and fitting of crystal electric field Hamiltonians*, Journal of Applied Crystallography **54**, 356 (2021).

[45] D. J. Wales and J. P. K. Doye, *Global Optimization by Basin-Hopping and the Lowest Energy Structures of Lennard-Jones Clusters Containing up to 110 Atoms*, The Journal of Physical Chemistry A **101**, 5111 (1997).

[46] J. Banda, B. K. Rai, H. Rosner, E. Morosan, C. Geibel, and M. Brando, *Crystalline electric field of Ce in trigonal symmetry:* $CeIr_3Ge_7$ *as a model case*, Phys. Rev. B **98**, 195120 (2018).

[47] M. Nandi, A. Thamizhavel, and S. K. Dhar, *Anisotropic magnetic properties of trigonal* $ErAl_2Ge_2$ *single crystal*, Journal of Physics: Condensed Matter **32**, 185803 (2020).

[48] O. A. Starykh, *Unusual ordered phases of highly frustrated magnets: a review*, Reports on Progress in Physics **78**, 052502 (2015).

[49] G. H. Wannier, *Antiferromagnetism. The Triangular Ising Net*, Phys. Rev. **79**, 357 (1950).

[50] G. H. Wannier, *Antiferromagnetism. The Triangular Ising Net*, Phys. Rev. B **7**, 5017 (1973).

[51] N. D. Mermin and H. Wagner, *Absence of Ferromagnetism or Antiferromagnetism in One- or Two-Dimensional Isotropic Heisenberg Models*, Phys. Rev. Lett. **17**, 1133 (1966).

[52] N. D. Mermin and H. Wagner, *Absence of Ferromagnetism or Antiferromagnetism in One- or Two-Dimensional Isotropic Heisenberg Models*, Phys. Rev. Lett. **17**, 1307 (1966).

[53] P. Anderson, *Resonating valence bonds: A new kind of insulator?*, Materials Research Bulletin **8**, 153 (1973).

[54] D. H. Lee, J. D. Joannopoulos, J. W. Negele, and D. P. Landau, *Symmetry analysis and Monte Carlo study of a frustrated antiferromagnetic planar (XY) model in two dimensions*, Phys. Rev. B **33**, 450 (1986).

[55] W.-J. Hu, S.-S. Gong, W. Zhu, and D. N. Sheng, *Competing spin-liquid states in the spin-$\frac{1}{2}$ Heisenberg model on the triangular lattice*, Phys. Rev. B **92**, 140403 (2015).

[56] Y.-D. Li, X. Wang, and G. Chen, *Anisotropic spin model of strong spin-orbit-coupled triangular antiferromagnets*, Phys. Rev. B **94**, 035107 (2016).

[57] Y. Iqbal, W.-J. Hu, R. Thomale, D. Poilblanc, and F. Becca, *Spin liquid nature in the Heisenberg $J_1 - J_2$ triangular antiferromagnet*, Phys. Rev. B **93**, 144411 (2016).

[58] S.-S. Gong, W. Zhu, J.-X. Zhu, D. N. Sheng, and K. Yang, *Global phase diagram and quantum spin liquids in a spin-$\frac{1}{2}$ triangular antiferromagnet*, Phys. Rev. B **96**, 075116 (2017).

[59] Z. Zhu, P. A. Maksimov, S. R. White, and A. L. Chernyshev, *Topography of Spin Liquids on a Triangular Lattice*, Phys. Rev. Lett. **120**, 207203 (2018).

[60] J. G. Rau and M. J. P. Gingras, *Frustration and anisotropic exchange in ytterbium magnets with edge-shared octahedra*, Phys. Rev. B **98**, 054408 (2018).

[61] Y. Li, G. Chen, W. Tong, L. Pi, J. Liu, Z. Yang, X. Wang, and Q. Zhang, *Rare-Earth Triangular Lattice Spin Liquid: A Single-Crystal Study of* $YbMgGaO_4$, Phys. Rev. Lett. **115**, 167203 (2015).

[62] Y. Shen, Y.-D. Li, H. Wo, Y. Li, S. Shen, B. Pan, Q. Wang, H. Walker, P. Steffens, M. Boehm, Y. Hao, D. L. Quintero-Castro, L. W. Harriger, M. D. Frontzek, L. Hao, S. Meng, Q. Zhang, G. Chen, and J. Zhao, *Evidence for a spinon Fermi surface in a triangular-lattice quantum-spin-liquid candidate*, Nature **540**, 559 (2016).

[63] Y. Li, D. Adroja, P. K. Biswas, P. J. Baker, Q. Zhang, J. Liu, A. A. Tsirlin, P. Gegenwart, and Q. Zhang, *Muon Spin Relaxation Evidence for the U(1) Quantum Spin-Liquid Ground State in the Triangular Antiferromagnet* $YbMgGaO_4$, Phys. Rev. Lett. **117**, 097201 (2016).

[64] J. A. Paddison, M. Daum, Z. Dun, G. Ehlers, Y. Liu, M. B. Stone, H. Zhou, and M. Mourigal, *Continuous excitations of the triangular-lattice quantum spin liquid* $YbMgGaO_4$, Nature Physics **13**, 117 (2017).

[65] M. Baenitz, P. Schlender, J. Sichelschmidt, Y. A. Onykiienko, Z. Zangeneh, K. M. Ranjith, R. Sarkar, L. Hozoi, H. C. Walker, J.-C. Orain, H. Yasuoka, J. van den Brink, H. H. Klauss, D. S. Inosov, and T. Doert, $NaYbS_2$*: A planar spin-$\frac{1}{2}$ triangular-lattice magnet and putative spin liquid*, Phys. Rev. B **98**, 220409 (2018).

[66] J. Sichelschmidt, P. Schlender, B. Schmidt, M. Baenitz, and T. Doert, *Electron spin resonance on the spin-1/2 triangular magnet* $NaYbS_2$, Journal of Physics: Condensed Matter **31**, 205601 (2019).

[67] A. Ochiai, T. Inukai, T. Matsumura, A. Oyamada, and K. Katoh, *Spin Gap State of S = 1/2 Heisenberg Antiferromagnet* $YbAl_3C_3$, Journal of the Physical Society of Japan **76**, 123703 (2007).

[68] Y. Kato, M. Kosaka, H. Nowatari, Y. Saiga, A. Yamada, T. Kobiyama, S. Katano, K. Ohoyama, H. S. Suzuki, N. Aso, and K. Iwasa, *Spin-Singlet Ground State in the Two-Dimensional Frustrated Triangular Lattice: $YbAl_3C_3$*, Journal of the Physical Society of Japan **77**, 053701 (2008).

[69] A. Ochiai, K. Hara, F. Kikuchi, T. Inukai, E. Matsuoka, H. Onodera, S. Nakamura, T. Nojima, and K. Katoh, *Quantum spin system in f-electron compounds – $YbAl_3C_3$ and its related compounds*, Journal of Physics: Conference Series **200**, 022040 (2010).

[70] K. Hara, S. Matsuda, E. Matsuoka, K. Tanigaki, A. Ochiai, S. Nakamura, T. Nojima, and K. Katoh, *Quantum spin state in the rare-earth compound $YbAl_3C_3$*, Phys. Rev. B **85**, 144416 (2012).

[71] Y. Liu, S. Zhang, J. Lv, S. Su, T. Dong, G. Chen, and N. Wang, *Revealing a Triangular Lattice Ising Antiferromagnet in a Single-Crystal $CeCd_3As_3$*, arXiv preprint arXiv:1612.03720 (2016).

[72] S. R. Dunsiger, J. Lee, J. E. Sonier, and E. D. Mun, *Long-range magnetic order in the anisotropic triangular lattice system* $CeCd_3As_3$, Phys. Rev. B **102**, 064405 (2020).

[73] K. E. Avers, P. A. Maksimov, P. F. S. Rosa, S. M. Thomas, J. D. Thompson, W. P. Halperin, R. Movshovich, and A. L. Chernyshev, *Fingerprinting triangular-lattice antiferromagnet by excitation gaps*, Phys. Rev. B **103**, L180406 (2021).

[74] S. Higuchi, Y. Noshima, N. Shirakawa, M. Tsubota, and J. Kitagawa, *Optical, transport and magnetic properties of new compound $CeCd_3P_3$*, Materials Research Express **3**, 056101 (2016).

[75] J. Lee, A. Rabus, N. R. Lee-Hone, D. M. Broun, and E. Mun, *The two-dimensional metallic triangular lattice antiferromagnet* $CeCd_3P_3$, Phys. Rev. B **99**, 245159 (2019).

[76] S. S. Stoyko and A. Mar, *Ternary Rare-Earth Arsenides $REZn_3As_3$ (RE = La–Nd, Sm) and $RECd_3As_3$ (RE = La–Pr)*, Inorganic Chemistry **50**, 11152 (2011).

[77] A. Ochiai, N. Kabeya, K. Maniwa, M. Saito, S. Nakamura, and K. Katoh, *Field-induced anomalous magnetic state beyond the magnetically ordered state in the slightly distorted triangular $S = \frac{1}{2}$ rare-earth antiferromagnet* $CeZn_3P_3$, Phys. Rev. B **104**, 144420 (2021).

[78] C. L. Huang, V. Fritsch, B. Pilawa, C. C. Yang, M. Merz, and H. v. Löhneysen, *Low-temperature magnetic, thermodynamic, and transport properties of antiferromagnetic CeAuSn single crystals*, Phys. Rev. B **91**, 144413 (2015).

[79] S. Shin, V. Pomjakushin, L. Keller, P. F. S. Rosa, U. Stuhr, C. Niedermayer, R. Sibille, S. Toth, J. Kim, H. Jang, S.-K. Son, H.-O. Lee, T. Shang, M. Medarde, E. D. Bauer, M. Kenzelmann, and T. Park, *Magnetic structure and crystalline electric field effects in the triangular antiferromagnet* $CePtAl_4Ge_2$, Phys. Rev. B **101**, 224421 (2020).

[80] P. G. Pagliuso, D. J. Garcia, E. Miranda, E. Granado, R. Lora Serrano, C. Giles, J. G. S. Duque, R. R. Urbano, C. Rettori, J. D. Thompson, M. F. Hundley, and J. L. Sarrao, *Evolution of the magnetic properties and magnetic structures along the R_mMIn_{3m+2} (R=Ce, Nd, Gd, Tb; M=Rh, Ir; and m=1,2) series of intermetallic compounds*, Journal of Applied Physics **99**, 08P703 (2006).

[81] D. T. Adroja, B. D. Rainford, and A. J. Neville, *Crystal fields and spin dynamics of hexagonal CeTSn compounds (T = Cu, Ag and Au)*, Journal of Physics: Condensed Matter **9**, L391 (1997).

[82] W. K. Robinson and S. A. Friedberg, *Specific Heats of* $Ni\mathrm{Cl}_2 \cdot 6\mathrm{H}_2O$ *and* $Co\mathrm{Cl}_2 \cdot 6\mathrm{H}_2O$ *between 1.4° and 20°K*, Phys. Rev. **117**, 402 (1960).

[83] L. Seabra, T. Momoi, P. Sindzingre, and N. Shannon, *Phase diagram of the classical Heisenberg antiferromagnet on a triangular lattice in an applied magnetic field*, Phys. Rev. B **84**, 214418 (2011).